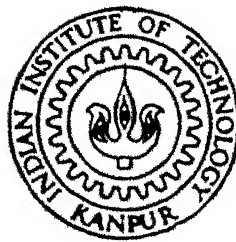


4/10/924

# MODELING OF SUBSTRATE CURRENT AND TRANSCONDUCTANCE OVERSHOOT IN ULTRA-SHORT CHANNEL MOSFETS

by

Jay Sudhir Kolhatkar



H  
E/1999/M  
832m

DEPARTMENT OF ELECTRICAL ENGINEERING  
**INDIAN INSTITUTE OF TECHNOLOGY KANPUR**

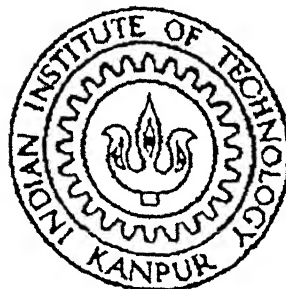
February, 1999

# MODELING OF SUBSTRATE CURRENT AND TRANSCONDUCTANCE OVERSHOOT IN ULTRA-SHORT CHANNEL MOSFETS

*A Thesis submitted  
in Partial Fulfillment of the Requirements  
for the degree of*

**Master of Technology**

*by*  
**Jay Sudhir Kolhatkar**



to the  
**DEPARTMENT OF ELECTRICAL ENGINEERING  
INDIAN INSTITUTE OF TECHNOLOGY, KANPUR**

*February 1999*

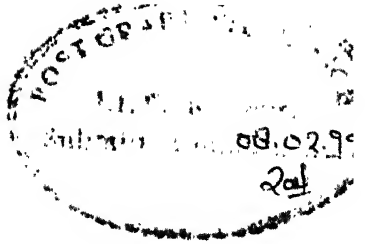
01 APR 1999 /E/

CENTRAL LIBRARY  
I.I.T., KANPUR

No. A 127830



A127830



# Certificate

This is to certify that the work contained in the thesis entitled "Modeling of Substrate Current and Transconductance Overshoot in Ultra-Short Channel MOSFETs" by **Jay Sudhir Kolhatkar** has been carried out under my supervision and that this work has not been submitted elsewhere for the award of a degree.

(Dr. Aloke Dutta)

Associate Professor

Department of Electrical Engineering,  
Indian Institute of Technology, Kanpur  
February 1999.

# Acknowledgements

I take this opportunity to express my sincere gratitude towards my thesis supervisor, Dr. Aloke Dutta, for his invaluable guidance and for the pains he has taken in the preparation of this report. Working under him has been a rewarding experience for me.

I would like to express my sincere regards to my professors Dr. M. B. Patil, Dr. S. Kar, Dr. Subir Roy, and Dr. R. Sharan. I would also like to thank IIT Kanpur, for providing excellent computing facilities, without which the completion of this thesis would not have been possible.

I would like to thank my course mates Pawan, Ravi, Sqn. Ldr. Ramesh, Mrs. Kulkarni, Karthik, and Ashokji for their constant support and company. And finally my stay at IIT Kanpur wouldn't be the same, had it not been for my D-mid wing-mates Ritesh, Goutamda, Jalda, Samarjit, Himadri, Pratul, Arindam, and Sandy.

Jay Sudhir Kolhatkar

# Abstract

Rapid developments in the fabrication technology have resulted in the scaling down of MOSFET device dimensions to ultra-small feature sizes. Thus, MOSFET models which accurately incorporate the various short-channel effects, are becoming important. The abnormal increase observed in the transconductance of ultra-short channel length MOSFETs is one such phenomenon which needs to be modeled accurately, as the transconductance parameter of the MOSFET is extremely important from analog as well as digital circuit point of view. Previous authors have modeled this abnormal increase in the transconductance by assuming that there is an overshoot of the electron velocity beyond the saturation value in Silicon for ultra-short channel length devices. However, in their models, they assumed that the mobility is pinned to its low-field value, which is highly inaccurate, since the electric field present in the channel for ultra-short channel length MOSFETs is very large, and the assumption of the low-field mobility to be applicable for such high channel fields may not hold true. In this work, the abnormal increase in the transconductance with decreasing channel lengths has been accounted for by proposing a new expression for the electron mobility, which is a function of the critical electric field, the channel length, the oxide thickness, the applied drain-to-source voltage, and the applied gate-to-source voltage. The results obtained

from our model have been compared with those reported experimentally, and a good match between the two is seen.

Another effect which becomes significant with shrinking device dimensions is the substrate leakage current caused by the impact ionization of high energy carriers in the surface depletion region near the drain. Previous authors have modeled the ionization length near the drain in a totally empirical manner. In this work, a simple and accurate approximation of the ionization length, based on a calculation of the electric field distribution near the drain region has been developed. Our model results are compared with the experimental results reported in literature and a good correlation between the two is obtained. This improved model for the ionization length has been used in the substrate current model developed in this work. A comparison of our simulation results with the ones reported experimentally shows a good match between the two. Prior to modeling these ultra-short channel effects, an existing physics based MOSFET model available in literature is simulated in order to gain a better understanding of MOSFET device physics and simulation problems.

# Contents

<b>List of Figures</b>	iii
<b>List of Tables</b>	viii
<b>1 Introduction</b>	1
<b>2 A Physics Based MOSFET Model</b>	7
2.1 Introduction . . . . .	7
2.2 The Static Drain Current Model . . . . .	8
2.3 Analysis and Results . . . . .	22
<b>3 The Substrate Current Model</b>	31
3.1 Introduction . . . . .	31
3.2 Model Formulation . . . . .	32

3.3	Analysis and results . . . . .	38
<b>4</b>	<b>Transconductance Overshoot Model for Submicron MOSFETs</b>	<b>44</b>
4.1	Introduction . . . . .	44
4.2	Model Formulation . . . . .	48
4.3	Results and Discussion . . . . .	52
<b>5</b>	<b>Summary and Conclusions</b>	<b>61</b>
5.1	Summary of the work . . . . .	62
5.2	Scope for Improvement . . . . .	64
	<b>Bibliography</b>	<b>65</b>

# List of Figures

2.1	The details of a MOSFET structure showing the three regions A, B, and C, with $l_{satS}$ , $l_{lin}$ , and $l_{satD}$ being their respective lengths. . . . .	9
2.2	$I_D$ - $V_{DS}$ characteristics obtained from our simulation for $V_{BS} = 0$ V and different values of $V_{GS}$ for a MOSFET having channel length of 0.55 $\mu m$ and channel width of 25 $\mu m$ . The experimentally obtained results [8] are also shown for the sake of comparison. . . . .	23
2.3	$I_D$ - $V_{DS}$ characteristics obtained from our simulation for $V_{BS} = 0$ V and different values of $V_{GS}$ for a MOSFET having channel length of 25 $\mu m$ and channel width of 25 $\mu m$ . The experimentally obtained results [8] are also shown. . . . .	24
2.4	$I_D$ - $V_{GS}$ characteristics obtained from our simulation for $V_{DS} = 0.5$ V and different values of $V_{BS}$ for a MOSFET having channel length of 0.55 $\mu m$ and channel width of 25 $\mu m$ . The experimentally obtained results [8] are also shown for the sake of comparison.	25

2.5 $I_D$ - $V_{GS}$ characteristics obtained from our simulation for $V_{DS} = 0.5$ V and different values of $V_{BS}$ for a MOSFET having channel length of 25 $\mu m$ and channel width of 25 $\mu m$ . The experimentally obtained results [8] are also shown for the sake of comparison.	26
2.6 $g_m$ - $V_{GS}$ characteristics obtained from our simulation for $V_{BS} = 0$ V and $V_{DS} = 0.5$ V, for a MOSFET having channel length of 0.55 $\mu m$ and channel width of 25 $\mu m$ . The experimentally obtained results [8] are also shown for the sake of comparison.	27
2.7 $g_m$ - $V_{GS}$ characteristics obtained from our simulation for $V_{BS} = 0$ V and $V_{DS} = 0.5$ V, for a MOSFET having channel length of 25 $\mu m$ and channel width of 25 $\mu m$ . The experimentally obtained results [8] are also shown for the sake of comparison.	28
2.8 $g_{ds}$ - $V_{DS}$ characteristics obtained from our simulation for different values of $V_{GS}$ for $V_{BS} = 0$ V for a MOSFET having channel length of 0.55 $\mu m$ and channel width of 25 $\mu m$ . The experimentally obtained results [8] are also shown for the sake of comparison.	29
2.9 $g_{ds}$ - $V_{DS}$ characteristics obtained from our simulation for different values of $V_{GS}$ for $V_{BS} = 0$ V for a MOSFET having channel length of 25 $\mu m$ and channel width of 25 $\mu m$ . The experimentally obtained results [8] are also shown and compared with our model results.	30

3.1	Figure showing the coordinate system, velocity saturation region, and boundary conditions, for evaluating the channel electric field $E(y)$ . . . . .	33
3.2	Ionization length $l_d$ as a function of $V_D - V_{Dsat}$ , for $L = 0.5 \mu m$ . Symbols indicate MINIMOS generated data [7]. . . . .	39
3.3	Ionization length $l_d$ as a function of the channel length $L$ , for $V_D - V_{Dsat} = 2.0 V$ and $2.5 V$ . Symbols indicate MINIMOS generated data [7]. . . . .	40
3.4	The values of $I_{sub}$ obtained from the approximate relation [Eqn.(3.15)], and the numerically integrated values obtained from the exact expression [Eqn.(3.11)] versus the gate-to-source voltage $V_{GS}$ , for three different channel lengths ( $0.5 \mu m$ , $0.6 \mu m$ , and $0.7 \mu m$ ). . . . .	41
3.5	The simulated values of the substrate current $I_{sub}$ obtained from our model as a function of the gate-to-source voltage $V_{GS}$ , for $V_{DS} = 4.6 V$ and $V_{BS} = 0 V$ . The experimental data reported by Arora and Sharma [6] are also shown for comparison. . . . .	42
4.1	Variation of the drift velocity of electrons with time, for different values of the electric field $E$ [18]. . . . .	45
4.2	Variation of the drift velocity of electrons as a function of distance from the source for different values of the electric field $E$ [18]. . . . .	46



- 4.6 The room temperature (300 K) and low temperature (77 K) overshoot factor  $F_v$  as a function of the channel length, as reported by Sai-Halasz *et al.* [1], shown by symbols. The results simulated from our model (lines) are also shown for comparison. The parameter values used in the simulation are  $V_{GS} - V_T = 0.6 \text{ V}$  and  $V_{DS} = 0.8 \text{ V}$ . The other parameter values are given in Table 4.3. . . . . 57
- 4.7 Extracted values of the parameter  $L_{co}$  (shown by symbols) as a function of the mobility  $\mu_G$  along with a straight line best fit. . . . . 59

# List of Tables

3.1	The values of the parameters needed for determining the substrate current $I_{sub}$ . . . . .	41
4.1	Extracted model parameter values obtained from a comparison of the results simulated from our model with experimental transconductance values reported by Sai-Halasz <i>et al.</i> [1]. . . . .	54
4.2	Extracted parameter values after comparison of our results with the simulated transconductance values reported by Pinto <i>et al.</i> [22]. . . . .	56
4.3	Extracted model parameter values after comparison of the overshoot factor simulated from our model with the reported values by Sai-Halasz <i>et al.</i> [1]. . . . .	56
4.4	Extracted values of the parameter $L_{co}$ for different values of $\mu_G$ . . . . .	58

# Chapter 1

## Introduction

Very Large Scale Integration (VLSI) is the assembly of millions of transistors on a single chip known as the Integrated Circuit (IC). One of the main reasons for the popularity of the VLSI systems is the advancements in the fabrication technology which resulted in a very high packing density, made possible by a reduction in the sizes of the individual transistors on the VLSI chip. The metal-oxide-semiconductor field-effect transistor (MOSFET) has emerged as the most important electronic device, superseding the bipolar junction transistor in sales volume and applications. Its strength derives from its simple structure, low fabrication cost, and low power dissipation. For these reasons, MOSFETs continue to be the most popular device for VLSI.

Computer Aided Design (CAD) and simulation of electronic circuits are the main factors contributing to the success of VLSI. For accurate simulation of the electronic circuits, the devices used in the circuits must be modeled accurately. Thus, device modeling becomes an essential step in computer aided design and simulation of electronic circuits.

The device model is a mathematical representation of the physical characteristics of the device. It is a set of mathematical equations which describe the physical behavior of the device under various input conditions. The set of parameters (constants) in these mathematical equations that represent the device phenomenon analytically are called the physical parameters, whereas the parameters which are used in the model equations such that these equations are the numerical approximations of the device behavior are known as the empirical parameters.

Development of models, which are totally based on the physical phenomenon, is a difficult task and also computationally very intensive. Although such models are highly accurate, they prove to be inefficient for circuit simulation. The totally empirical models, on the other hand, are computationally very efficient, however, they are less accurate and do not always give a true physical picture of events taking place within the device. With VLSI gaining popularity and device dimensions continuously shrinking, the existing MOSFET models, which hold their validity for long channel lengths, become grossly inadequate in properly simulating the device operation for submicron channel lengths. Therefore, some modifications of the existing models are necessary in order to accurately portray the electrical characteristics for such ultra-short devices. Some of the second order effects which are dominant in short channel devices are described below.

In short-channel devices, it is found that in the saturation region, there is an appreciable increase in the drain current  $I_D$  with an increase in the drain-to-source voltage  $V_{DS}$ , particularly so for very short channel length devices. This phenomenon is termed as the channel length modulation effect, and is caused by a variation in the effective channel length due to the applied  $V_{DS}$ .

This effect is either negligible or absent in long channel devices.

In the subthreshold region, the lowering of the source-channel potential barrier by the applied drain-to-source voltage in short channel devices is known as the Drain Induced Barrier Lowering (DIBL) effect. The immediate manifestation of this effect is an increase in the subthreshold current. In effect, the threshold voltage  $V_T$  becomes a function of the channel length  $L$  and the applied  $V_{DS}$ , with  $V_T$  reducing with a reduction in  $L$  and with an increase in  $V_{DS}$ . This phenomenon is totally absent in long channel devices.

Another important effect that comes into prominence with decreasing channel length is an abnormal increase in the device transconductance  $g_m$  for ultra-small channel length devices [1-4]. The reason given for this higher than theoretically predicted maximum values of  $g_m$  for ultra-small channel length devices, is the electron velocity overshoot [1-4]. In the model developed by Roldan *et al.* [5], an electron velocity overshoot parameter  $\lambda_a$  is used in order to model the carrier drift velocity  $v$  in the inhomogeneous electric field present in the channel. In the expression for the transconductance,  $\lambda_a$  accounts for the increase in the transconductance for ultra-small channel lengths, while assuming a constant value for the low-field electron mobility. This approximation of using the values for the low-field electron mobility for such high values of electric field present in the channel is grossly inaccurate.

Another effect which becomes significant when device dimensions are scaled down is the substrate leakage current caused by the impact ionization by high energy carriers. When a MOSFET is biased in the saturation region, a measurable substrate current  $I_{sub}$  always flows. This current is the result of the electron-hole pair generation in the surface depletion region near the drain due

to impact ionization. It is extremely sensitive to device dimensions, channel doping, terminal voltages, and temperature. In the substrate current model proposed by Arora and Sharma [6], the carrier ionization length  $l_d$  near the drain is modeled in a semi-empirical manner. Since the substrate current  $I_{sub}$  depends exponentially on this ionization length  $l_d$ , a small error in its calculation can lead to a large error in the computed value of  $I_{sub}$ . As  $l_d$  is modeled semi-empirically, there is no physical significance for the model parameters,  $l_0$ ,  $l_1$ , and  $l_2$  appearing in [6].

In this work, we have made an attempt to model the last two effects mentioned in the previous paragraphs, i.e., the transconductance overshoot and the substrate current in ultra-short channel length devices, in an analytical manner, based on device physics. However, since totally physical models are difficult to develop and are computationally inefficient, fitting parameters are used whenever required. A brief description of the work is given below.

The increase in the transconductance  $g_m$  with decreasing channel lengths has been accounted for in this work by proposing a new expression for the electron mobility, which is a function of the critical electric field, the channel length, the oxide thickness, the applied drain-to-source voltage  $V_{DS}$ , and the applied gate-to-source voltage  $V_{GS}$ . With large channel electric field and small channel length, the mobility is bound to increase, and the increase in the transconductance is then accounted for by the correspondingly enhanced electron mobility. Our model results are compared with those reported in literature, and they show a good match.

For the other effect, i.e., the substrate current due to impact ionization of high energy carriers, a simple and accurate approximation of the ionization

length  $l_d$ , based on a calculation of the electric field distribution near the drain region has been developed in this work. Our model results are compared with the MINIMOS simulation results reported by Wong and Poon [7], and a good correlation between the two is obtained. This new model for  $l_d$  is then used to calculate the substrate current. The results obtained from the improved substrate current model are then compared with the experimental data reported by Arora and Sharma [6], and a good match is obtained between the two.

However, before attempting to model these two effects for ultra-small channel length MOSFETs, an existing physics based MOSFET model, reported by Joardar *et al.* [8] is rederived and simulated in this work in order to gain a better feel for the MOSFET device physics and the simulation problems. A major drawback in the existing MOSFET models is the presence of discontinuities in the derivatives of the drain current with respect to the gate-to-source voltage and the drain-to-source voltage. These discontinuities arise primarily due to the nature of the velocity-field relations and the smoothing functions used in these models for the transition region between the linear and the saturation regions. The model developed by Joardar *et al.* [8] attempts to overcome these problems. The new model [8] is normalized surface potential based and is quasi-static in nature, i.e., the variation of the terminal voltages is assumed to be sufficiently slow, so that they can be assumed to be identical to the dc voltages at any given time. This model is simulated in our work and the results obtained are compared with the experimental values given by Joardar *et al.* [8].

The organization of this report is as follows. The rederivation and simulation of the physics based MOSFET model developed by Joardar *et al.* [8], and

the comparison of the simulated results with those reported [8] are presented in Chapter 2. In Chapter 3, the improved model for the ionization length  $l_d$  is given, which is used to obtain the improved substrate current model. This chapter also includes the comparison of the simulated model results with the experimental ones reported by Arora and Sharma [6]. The enhanced mobility model developed in this work is presented in Chapter 4. This chapter also includes the comparison of the transconductance values obtained from the expression derived in this work with the experimental transconductance values reported by Sai-Halasz *et al.* [1]. Finally, Chapter 5 includes the summary of the entire work. The shortcomings of the models developed in this work along with the future scope for improvement, are also discussed in this chapter.

# **Chapter 2**

## **A Physics Based MOSFET Model**

### **2.1 Introduction**

There have been many MOSFET models developed over the years. Most of these models have drawbacks stemming from simplifying assumptions made during their development. These drawbacks limit the accuracy of these models in specific regions of device operation. A major drawback is the presence of discontinuities in the derivatives of the drain current with respect to the gate-to-source voltage and the drain-to-source voltage of the MOSFET. These discontinuities arise primarily due to the nature of the velocity-field expressions and the smoothing functions used in the transition area between the linear and the saturation regions in these models. A compact model is presented by Joardar *et al.* [8], which overcomes the problems mentioned above. The new

new model is based on the normalized surface potential and is quasi-static in nature, i.e., the variation of the terminal voltages is assumed to be sufficiently slow, so that they can be assumed to be identical to the dc voltages at any given time.

In this chapter, the model developed by Joardar *et al.* [8] is rederived in order to get a better understanding of MOSFET device physics and the problems associated with device simulations. The simulated results obtained from the model are then compared with the experimental values reported by Joardar *et al.* [8].

## 2.2 The Static Drain Current Model

Consider an n-channel MOSFET with the structure as shown in Fig.2.1. The channel is divided into three sub-regions, namely A, B, and C, with lengths  $l_{satS}$ ,  $l_{lm}$ , and  $l_{satD}$  respectively. Let  $V_D$ ,  $V_G$ ,  $V_S$ , and  $V_B$  be the drain voltage, gate voltage, source voltage, and body voltage respectively. The regions A and C do not exist simultaneously, i.e., when  $V_D > V_S$ ,  $l_{satS}$  is zero and region A is absent; and when  $V_S > V_D$ ,  $l_{satD}$  is zero and region C is absent; and for  $V_D = V_S$ , both regions A and C vanish completely. The drain current  $I_D$  saturates as  $V_D$  increases above a certain threshold value  $V_{Dsat}$ . Therefore, in either of the regions A or C, the carriers are assumed to flow with the saturation velocity  $v_{sat}$ , depending upon whether  $V_S > V_D$  or  $V_S < V_D$  respectively. For  $V_D < V_{Dsat}$ ,  $I_D$  increases almost linearly with increasing  $V_D$  (for small values of  $V_D$ ). Thus, in region B, the carrier velocity is assumed to be less than  $v_{sat}$ .

The general expression for the drain current  $I_D$  can be written in terms of

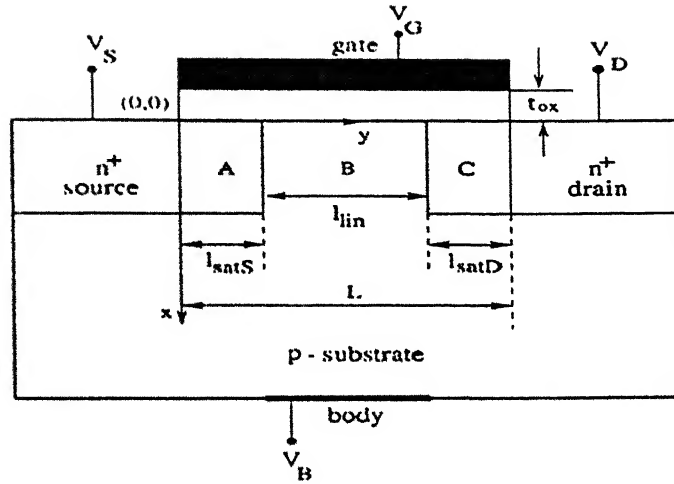


Figure 2.1: The details of a MOSFET structure showing the three regions A, B, and C, with  $l_{satS}$ ,  $l_{lin}$ , and  $l_{satD}$  being their respective lengths.

the drift and the diffusion components respectively [8]

$$I_D = -WvQ'_i + WD \frac{dQ'_i}{dy}, \quad (2.1)$$

where  $W$  is the effective channel width,  $v$  is the average carrier drift velocity,  $Q'_i$  represents the inversion charge density per unit area in the channel, and  $D$  is an effective diffusion constant. The normalized potential is defined as [8]

$$F_i(y) = Q'_i(y)/C'_{ox}, \quad (2.2)$$

where  $C'_{ox}$  is the oxide capacitance per unit area and is given by

$$C'_{ox} = \epsilon_{ox}/t_{ox}, \quad (2.3)$$

with  $\epsilon_{ox}$  and  $t_{ox}$  being the oxide permittivity and thickness respectively. Thus,

the current equation can be rewritten as [8]

$$I_D = -WC'_{ox}vF_i + WC'_{ox}D \frac{dF_i}{dy}. \quad (2.4)$$

The expression for the carrier velocity as a function of the lateral electric field can be given as [8]

$$v = \frac{\mu_{eff}(d\phi/dy)}{(1 + (\frac{\mu_{eff}}{v_{sat}} \frac{d\phi}{dy})^2)^{1/2}}, \quad (2.5)$$

where  $\phi(y)$  is the surface potential and  $d\phi/dy$  is the lateral electric field. The effective mobility  $\mu_{eff}$  can be given by [8]

$$\mu_{eff} = U_0/f_\mu, \quad (2.6)$$

where  $U_0$  is the low field mobility and  $f_\mu$  is the mobility degradation factor due to the vertical (gate) field. Equation (2.5) satisfies the necessary conditions for a sufficiently accurate velocity-field expression, and also represents the measured characteristics adequately [9]. The mobility degradation factor  $f_\mu$  is typically expressed in terms of the excess gate voltage beyond the threshold voltage. However, since this model [8] is surface potential based,  $f_\mu$  can be expressed in a more fundamental form as a function of the vertical electric field, and is given by the empirical relation [8]

$$f_\mu = 1 + UBRED(E_{av} \times 10^{-8})^{EAVEXP}, \quad (2.7)$$

where  $UBRED$  and  $EAVEXP$  are dimensionless model parameters, and  $E_{av}$

is the effective vertical electric field given by the expression [8]

$$E_{av} = (Q'_b + EAVFC'_{ox}F_i)\epsilon_{Si}, \quad (2.8)$$

where  $EAVF$  is another dimensionless fitting parameter,  $Q'_b$  is the depletion charge per unit area, and  $\epsilon_{Si}$  is the permittivity of Si. The form of this model for the vertical electric field induced mobility degradation is suggested by Sun and Plummer [10].

Following well known principles of MOS physics, the normalized potential  $F_i$  can be expressed as [8]

$$F_i(\phi) = V_{GB} - V_{FB} - \phi - Q'_b(\phi)/C'_{ox}, \quad (2.9)$$

where  $\phi$  is the surface potential,  $V_{GB}$  is the applied gate-to-bulk voltage, and  $V_{FB}$  is the flatband voltage. In the linear region, i.e.,  $V_{Dsat} > V_D > V_S$ , the regions *A* and *C* in Fig.2.1 are absent, and  $l_{satS} = l_{satD} = 0$ . At  $y = 0$  (i.e., at source), the exact values for the surface potential and the depletion charge per unit area are denoted by  $\phi_s$  and  $Q'_{bS}$  respectively. In the region  $0 \leq y \leq l_{lin}$ ,  $Q'_b$  can be approximately given by [8]

$$Q'_b \approx (Q'_{bS} + Q'_{bD})/2 + g\alpha(\phi - \phi_s/2 - \phi_D/2), \quad (2.10)$$

where  $Q'_{bD}$  and  $\phi_D$  are the depletion charge per unit area and the surface potential respectively at the drain end (i.e., at  $y = l_{lin}$ ),  $g$  is the dimensionless

Gummel's linearization factor and  $\alpha$  (C/V-cm<sup>2</sup>) is given as [11]

$$\alpha = \frac{1}{2} \left\{ \frac{dQ'_b}{d\phi} \Big|_{\phi=\phi_D} + \frac{dQ'_b}{d\phi} \Big|_{\phi=\phi_S} \right\}. \quad (2.11)$$

Equation(2.10) is derived in the following manner. First,  $Q'_b(\phi)$  is linearized by expanding it in Taylor series around  $\phi = \phi_S$ , and retaining only the first two terms. It is then similarly linearized around  $\phi = \phi_D$ . Finally, these two linearized versions of  $Q'_b$  are averaged in order to yield the given expression [Eqn.(2.10)]. Thus, the expression for the normalized potential  $F_i$  linearized in terms of the surface potential  $\phi$  can be given as [8]

$$F_i(\phi) \approx (F_{iS} + F_{iD})/2 - (1 + g\alpha)(\phi - \phi_S/2 - \phi_D/2), \quad (2.12)$$

where  $F_{iS}$  and  $F_{iD}$  are the exact values of  $F_i$  at the source and the drain respectively. Substituting these values in the expression for the drain current  $I_D$  [Eqn.(2.1)] and integrating, one obtains [8]

$$I_D = \frac{\mu_{effavg} C'_{ox} (W/L) [(F_{iS} + F_{iD})(\phi_D - \phi_S)/2 + V_{th}(F_{iS} - F_{iD})]}{(1 + (\frac{\mu_{effavg}(\phi_D - \phi_S)}{v_{sat}l_{lin}})^2)^{1/2} L_{red}}, \quad (2.13)$$

where  $V_{th}$  is the thermal voltage, given by  $V_{th} = kT/q$ , with  $k$  being the Boltzmann's constant,  $T$  being the absolute temperature, and  $q$  being the electronic charge,  $L_{red}$  is the channel length reduction factor, given by  $L_{red} = l_{lin}/L$ , with  $L$  being the total channel length, and  $l_{lin}$  bounding the ohmic region of the channel, as shown in Fig.2.1. In Eqn.(2.13), the effective mobility  $\mu_{eff}$  is replaced by another term  $\mu_{effavg}$ , which is an average of its values at

$y = 0$  and at  $y = l_{th}$  (given by  $\mu_{effS}$  and  $\mu_{effD}$  respectively), and is given by [8]

$$\mu_{effavg} = (\mu_{effS} + \mu_{effD})/2. \quad (2.14)$$

The first and the second terms in the numerator of Eqn.(2.13) are the drift and the diffusion components respectively. The relation between the surface potential  $\phi_S$ , the gate-to-bulk voltage  $V_{GB}$ , and the source-to-bulk voltage  $V_{SB}$  can be given by [8]

$$V_{GB} = V_{FB} + \phi_S + \gamma_{eff} A, \quad (2.15)$$

with [8]

$$A = \sqrt{\phi_S(1 - e^{-\phi_i/V_{th}}) + V_{th}(e^{-\phi_S/V_{th}} + e^{(\phi_S - \phi_i - V_{SB})/V_{th}} - e^{-(\phi_i + V_{SB})/V_{th}} - 1)}, \quad (2.16)$$

where  $\gamma_{eff}$  is the effective value of the body-effect coefficient, and is a function of the channel doping and the oxide thickness, and  $\phi_i$  is the surface potential at the onset of strong inversion given by

$$\phi_i = 2V_{th} \ln(N_A/n_i), \quad (2.17)$$

where  $N_A$  is the substrate doping and  $n_i$  is the intrinsic carrier concentration. In this model,  $\gamma_{eff}$  has been expressed as [8]

$$\gamma_{eff}^2 = \frac{2q\epsilon_{si}N_{eff}}{C_{ox}'^2} e^{(CS1LL \times L^{CS1LE} + CS1WL \times W^{CS1WE})}, \quad (2.18)$$

where  $CS1LL$ ,  $CS1LE$ ,  $CS1WL$ , and  $CS1WE$  are fitting parameters necessary to model  $\gamma_{eff}$  over a wide range of geometries. This equation is solved using an iterative numerical approach similar to the Newton-Raphson algorithm. Once  $\phi_S$  is determined, the depletion charge  $Q'_{bs}$  and the normalized potential  $F_{is}$  are obtained by the following two equations

$$Q'_{bs} = \gamma_{eff} C'_{ox} \sqrt{\phi_S + V_{th} e^{-\phi_S/V_{th}} - V_{th}}, \quad (2.19)$$

and

$$F_{is} = V_{GB} - V_{FB} - \phi_S - Q'_{bs}/C'_{ox}. \quad (2.20)$$

These values are then substituted for  $Q'_b$  and  $F_i$  in order to get  $E_{av}$  at the source [Eqn.(2.8)]. This result is then used in Eqns.(2.6) and (2.7) in order to calculate the value of the effective mobility  $\mu_{effs}$ . In order to evaluate the surface potential  $\phi_D$  and the related quantities such as the inversion charge, etc., at the drain end of the ohmic region (i.e., at  $y = l_{in}$ ), the effective drain voltage  $V_{D1}$  at this location must be determined first. If terminal biases are such that the device operates in the traditional linear region, then  $V_{D1}$  is essentially equal to  $V_D$ , ignoring series resistance effects. On the other hand, in the saturation region,  $V_{D1}$  is pinned to the saturation voltage  $V_{Dsat}$ , which represents the electrical boundary between the linear and the saturation regions.  $V_{Dsat}$  is the value of  $V_D$  at which the mobile carrier velocity attains the thermal saturation velocity, equal to  $v_{sat}$ , at the pinch-off point of the channel.

With a fixed gate bias  $V_G$ , as the drain voltage is increased, the inversion charge density  $Q'_{iD}$  at the drain decreases, and the potential across the channel adjusts in order to increase the carrier velocity at the drain end so that the current flow is maintained. There is a limit as to how far  $Q'_{iD}$  can decrease, since

the maximum carrier drift velocity possible is equal to the thermal saturation velocity  $v_{sat}$ .

Once  $V_D$  is large enough, so that the maximum carrier drift velocity  $v_{sat}$  is reached,  $Q'_{iD}$  gets pinned at its minimum value, and the surface potential at the drain gets pinned at its maximum value  $\phi_{Dmax}$ . The drain voltage corresponding to this potential is equal to  $V_{Dsat}$ . As  $V_D$  increases beyond  $V_{Dsat}$ , the region C, shown in Fig.2.1, is formed.

The excess drain voltage  $\Delta V_D$  ( $\doteq V_D - V_{Dsat}$ ) is dropped across this velocity saturated region. The length of this region  $l_{satD}$  increases with  $\Delta V_D$ , resulting in a finite output resistance.  $V_{Dsat}$  is obtained by equating the carrier velocity  $v$  at the drain end to be equal to  $v_{sat}$ . Thus [8]

$$v = \frac{I_D}{WF_{iD}C'_{ox}}, \quad (2.21)$$

where  $F_{iD}$  is the normalized inversion potential at the drain end, given by

$$F_{iD} = Q'_{iD}/C'_{ox}. \quad (2.22)$$

The expression for the drain current is given by Eqn.(2.13). In order to obtain a closed form solution for  $V_{Dsat}$ , the following approximations are made in Eqn.(2.13). The square root term in the denominator of Eqn.(2.13) is assumed to be equal to unity, and  $\mu_{effavg}$  is replaced by an effective mobility at the source end,  $\mu_{effS}$ . These approximations are valid since the potential drop across the ohmic region of the channel is usually not very high. At  $V_D = V_{Dsat}$ ,  $\phi_D = \phi_{Dmax}$  and the factor  $L_{red}$  is exactly equal to unity since the length of the velocity saturated region is still equal to zero. The carrier velocity at the

drain end can be expressed as [8]

$$v = v_{sat} = \frac{B}{WF_{IDmin}C'_{ox}}, \quad (2.23)$$

with

$$B = \mu_{eff}S C'_{ox} (W/L) [(F_{IS} + F_{IDmin})(\phi_{Dmax} - \phi_S)/2 + V_{th}(F_{IS} - F_{IDmin})], \quad (2.24)$$

where  $F_{IDmin}$  is the minimum normalized potential required at the drain end in order to sustain the current  $I_D$ .  $F_{IDmin}$  is related to  $\phi_{Dmax}$  by the following expression [8]

$$F_{IDmin} = V_{GB} - V_{FB} - \phi_{Dmax} - \gamma_{eff} \sqrt{\phi_{Dmax} + V_{th}e^{-\phi_{Dmax}/V_{th}} - V_{th}}. \quad (2.25)$$

Solving Eqn.(2.23), one gets a quartic equation for  $\phi_{Dmax}$  of the following form [8]

$$a\phi_{Dmax}^4 + b\phi_{Dmax}^3 + c\phi_{Dmax}^2 + d\phi_{Dmax} + e = 0, \quad (2.26)$$

where the coefficients are given by the following equations [8]

$$a = a_1^2, \quad (2.26.a)$$

$$b = -(2a_1b_1 + \gamma_{eff}^2 a_1^2), \quad (2.26.b)$$

$$c = b_1^2 + 2a_1c_1 + 2\gamma_{eff}^2 a_1c_2 + V_{th}\gamma_{eff}^2 a_1^2, \quad (2.26.c)$$

$$d = -(2b_1c_1 + \gamma_{eff}^2 c_2^2 + 2V_{th}\gamma_{eff}^2 a_1c_2), \quad (2.26.d)$$

$$c = c_1^2 + V_{th} \gamma_{eff}^2 c_2^2, \quad (2.26.e)$$

$$a_1 = \mu_{effS} / (2L v_{sat}), \quad (2.26.f)$$

$$b_1 = V_{Geff} a_1 + \phi_S a_1 + 2V_{th} a_1 + F_{iS} a_1, \quad (2.26.g)$$

$$c_1 = V_{Geff} + V_{Geff} \phi_S a_1 + 2V_{th} V_{Geff} a_1 + F_{iS} \phi_S a_1 - 2V_{th} F_{iS} a_1, \quad (2.26.h)$$

$$c_2 = 1 + \phi_S a_1 + 2V_{th} a_1, \quad (2.26.i)$$

and

$$V_{Geff} = V_{GB} - V_{FB}. \quad (2.26.j)$$

These equations are solved numerically and the root lying between  $\phi_S$  and  $\phi_S + V_{DB}$  is chosen, which gives the value of  $\phi_{Dmax}$ , the maximum possible value of the surface potential at the drain end. Obviously, the value of  $\phi_{Dmax}$  must lie between the surface potential at the source end  $\phi_S$  and  $\phi_S + V_{DB}$ , where  $V_{DB}$  is the drain-substrate voltage.

In order to find  $V_{Dsat}$ , the following equation is used [8]

$$V_{DBsat} = \phi_{Dmax} - \phi_i - V_{th} \ln \left\{ \frac{1}{V_{th}} \left[ ((V_{Geff} - \phi_{Dmax}) / \gamma_{eff})^2 - \phi_{Dmax} \right] - e^{-\phi_{Dmax}/V_{th}} + 1 \right\}, \quad (2.27)$$

where  $V_{DBsat} = V_{Dsat} - V_B$ . The assumption that  $\phi_{Dmax}$  is much larger than  $V_{th}$  may not be satisfied in weak inversion. However, in this case,  $V_{Dsat}$  can be obtained very simply by noting the following two points. First, for  $V_{DS} = V_{DSSat}$  (where  $V_{DSSat} = V_{Dsat} - V_S$ ), the drain current is given by [8]

$$I_D = W C'_{ox} F_{iD} v_{sat}, \quad (2.28)$$

and also, the drain current at the subthreshold region can be expressed by [11]

$$I_D = \frac{W}{L} \mu_{eff} V_{th} C'_{ox} F_{IS} (1 - e^{-V_{DSsat}/V_{th}}). \quad (2.29)$$

The ratio  $F_{ID}/F_{IS}$  is given as  $e^{-V_{DSsat}/V_{th}}$  [11]. Using these relations (i.e., Eqns.(2.28) and (2.29)),  $V_{DSsat}$  is obtained as  $V_{DSsat} = V_{th} \ln [1 + (v_{sat} L) / (\mu_{eff} V_{th})]$ , from which  $V_{Dsat}$  can be obtained by adding  $V_S$  to it. With the saturation voltage  $V_{Dsat}$  being known, the effective drain voltage  $V_{D1}$  can be found from the following equation [8]

$$V_{D1} = \frac{V_D - V_S}{(1 + ((V_D - V_S)/V_{Dsat})^{2\kappa})^{1/2\kappa}} + V_S, \quad (2.30)$$

where  $\kappa$  is an empirical fitting parameter [8]. After  $V_{D1}$  is determined, all the other drain side quantities can be found in a manner analogous to that applied for the source side. The drain end surface potential can be obtained by solving the following equation [8]

$$V_{GB} = V_{FB} + \phi_D + \gamma_{eff} A, \quad (2.31)$$

where

$$A = \sqrt{\phi_D (1 - e^{-\phi_i/V_{th}}) + V_{th} (e^{-\phi_D/V_{th}} + e^{(\phi_D - \phi_i - V_{D1B})/V_{th}} - e^{-(\phi_i + V_{D1B})/V_{th}} - 1)}, \quad (2.32)$$

where  $V_{D1B}$  is given by  $V_{D1B} = V_{D1} - V_B$ . The drain end depletion charge per unit area  $Q'_{bD}$  can be computed from the following expression [8]

$$Q'_{bD} = \gamma_{eff} C'_{ox} \sqrt{\phi_D + V_{th} e^{-\phi_D/V_{th}} - V_{th}}, \quad (2.33)$$

and the normalized potential at the drain end  $F_{iD}$  can be given by [8]

$$F_{iD} = V_{GB} - V_{FB} - \phi_D - Q'_{bD}/C'_{ox}. \quad (2.34)$$

The effective mobility at the drain end  $\mu_{effD}$  can then be calculated by substituting the expressions for  $Q'_{bD}$  and  $F_{iD}$  [Eqns.(2.33) and (2.34) respectively] for  $Q'_b$  and  $F_i$  respectively in Eqn.(2.8), and using Eqns.(2.6) and (2.7). The effective average mobility  $\mu_{effavg}$  can then be calculated by substituting  $\mu_{effS}$  and  $\mu_{effD}$  in Eqn.(2.14).

The length of the saturated portion of the channel  $l_{satD}$ , as reported in Fig.2.1, is obtained from a pseudo-two-dimensional analysis of this region as shown by El-Mansy and Boothroyd [12]. The solution of the two-dimensional Poisson's equation for the surface potential  $\phi_y$  in the velocity saturated region gives [12]

$$\phi_y = \phi_D + E_{sat} D_{ceff} \sinh\left(\frac{y - L_{red}L}{D_{ceff}}\right). \quad (2.35)$$

where  $D_{ceff}$  is the characteristic length which approximately represents the depth over which the mobile charge is spread in this region, and  $E_{sat}$  represents the lateral electric field at the boundary between the ohmic and the saturated regions of the channel, which can be expressed as  $E_{sat} = v_{sat}/\mu_0$ , with  $\mu_0$  being the low-field mobility. At the drain end, i.e., at  $y = L$ , the surface potential can be given by

$$\phi_y = \phi_D + (V_D - V_{D1}). \quad (2.36)$$

Substituting Eqn.(2.36) in Eqn.(2.35), we get expression for  $L_{red}$ , given by

$$L_{red} = 1 - \frac{D_{ceff}}{L} \sinh^{-1} \left( \frac{V_D - V_{D1}}{E_{sat} D_{ceff}} \right). \quad (2.37)$$

Replacing the inverse hyperbolic sine function by its logarithmic equivalent and by using the approximation  $\tanh(x) \approx x$  for  $x \ll 1$ , Eqn.(2.37) gets modified to [8]

$$L_{red} = 1 - \tanh \left[ \ln(a + \sqrt{1 + a^2})^{D_{ceff}/L} \right], \quad (2.38)$$

where  $a = (V_D - V_{D1})/(E_{sat} D_{ceff})$ . Equation (2.38) is of the form  $1 - \tanh(x)$ , which can be simplified as

$$1 - \tanh(x) = 1 - \frac{e^x - e^{-x}}{e^x + e^{-x}} = \frac{2}{e^{2x} + 1}. \quad (2.39)$$

Therefore, Eqn.(2.38) can be reduced to

$$L_{red} = \frac{2}{(a + \sqrt{1 + a^2})^{2D_{ceff}/L} + 1}. \quad (2.40)$$

The parameter  $D_{ceff}$  is known to be a function of the gate oxide thickness, doping density, drain junction depth, and applied bias [8]. Larger the gate field, the more strongly the carriers are accumulated near the surface resulting in a reduction in  $D_{ceff}$ . In this model,  $D_{ceff}$  has been expressed empirically as [8]

$$D_{ceff} = \sqrt{\frac{\epsilon_{si} t_{ox}}{\epsilon_{ox}}} \frac{LCL}{1 + LC1(F_{iS} - F_{iD})Q'_{BS}/C'_{ox}}, \quad (2.41)$$

where  $\epsilon_{si}$  is the permitivitty for Si and  $LCL$  and  $LC1$  are empirical model parameters having the units of  $cm^{1/2}$  and  $V^{-2}$  respectively.

In small geometry devices, it is important to model the Drain-Induced Barrier Lowering (DIBL) effect, which causes the surface potential at the source to be altered due to its proximity to the drain-substrate junction. Similarly, the surface potential at the drain is also affected by the state of the source-substrate junction. It causes the threshold voltage of a MOSFET to decrease as the reverse bias on the drain is increased. This results in an increase in the drain saturation current and a reduction in the output resistance as the drain bias is increased. In existing threshold voltage models, the DIBL effect is accounted for by making the threshold voltage  $V_T$  a function of  $V_{DS}$  [8], related by the following equation

$$V_T = V_{THO} - \sigma V_{DS}, \quad (2.42)$$

where  $V_{THO}$  is the threshold voltage in the absence of the DIBL effect, and  $\sigma$  is a parameter that controls the extent to which  $V_T$  is modulated by  $V_{DS}$ .

The present model accounts for the DIBL effect in the following manner. The surface potentials at the source and the drain ends are computed in the same manner as given earlier with the exception that  $V_{GB}$  is replaced by  $V_{GB} + K_{dibl}V_{DB}$  and by  $V_{GB} + K_{dibl}V_{SB}$  respectively, where  $K_{dibl}$  is a model parameter. The DIBL effect cannot be modeled accurately using a single value for  $K_{dibl}$  that is adequate for all values of channel length  $L$ , since this effect increases exponentially with decreasing channel length [13]. In the present work,  $K_{dibl}$  has been modeled as [8]

$$K_{dibl} = DIBLL \times L^{DIBLE}, \quad (2.43)$$

where  $DIBLL$  and  $DIBLE$  are model parameters, and depend on the particular device geometry.

The simulation results and their comparison with the experimentally obtained results are presented in the next section.

## 2.3 Analysis and Results

The simulated model results are compared with the measured data available in literature for long channel ( $L = 25 \mu m$ ) [8] and for short channel ( $L = 0.55 \mu m$ ) MOSFETs [8].

The simulated drain current ( $I_D$ ) versus the drain-to-source voltage ( $V_{DS}$ ) characteristics obtained from the model for different values of the gate-to-source voltage ( $V_{GS}$ ) are shown in Figs.2.2 and 2.3 for the body-to-source voltage  $V_{BS} = 0 V$  for two MOSFETs having channel lengths of  $0.55 \mu m$  and  $25 \mu m$  respectively. The experimental data reported by Joardar *et al.* [8] are also shown for comparison. The results show a good match between the two.

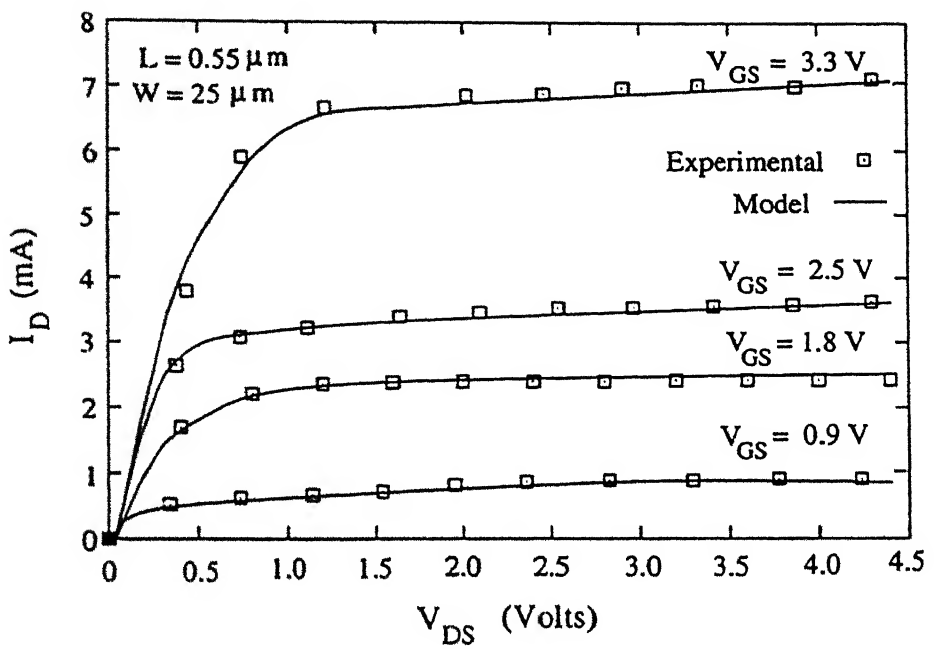


Figure 2.2:  $I_D$ - $V_{DS}$  characteristics obtained from our simulation for  $V_{BS} = 0 \text{ V}$  and different values of  $V_{GS}$  for a MOSFET having channel length of  $0.55 \mu m$  and channel width of  $25 \mu m$ . The experimentally obtained results [8] are also shown for the sake of comparison.

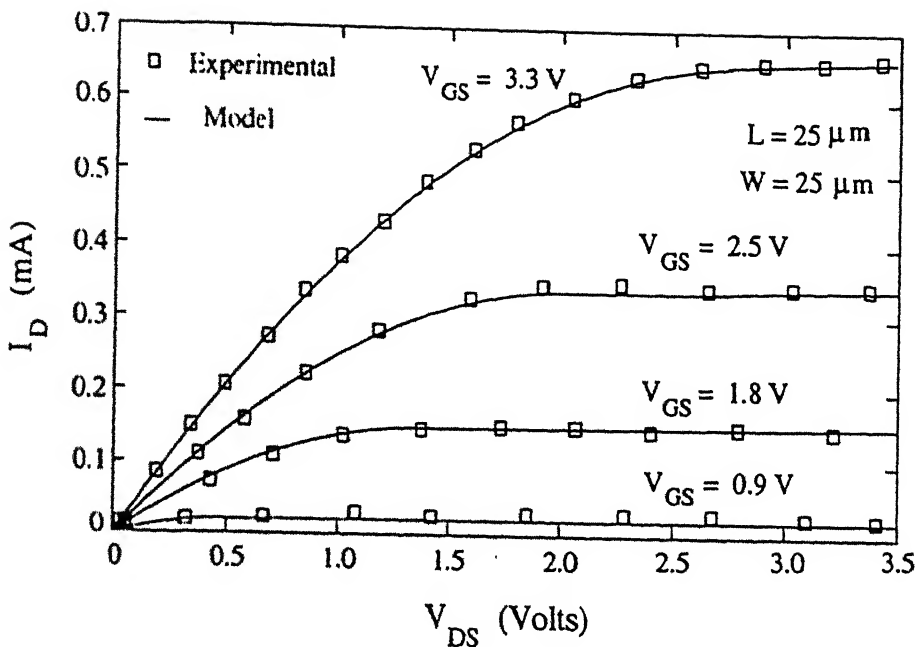


Figure 2.3:  $I_D$ - $V_{DS}$  characteristics obtained from our simulation for  $V_{BS} = 0\text{ V}$  and different values of  $V_{GS}$  for a MOSFET having channel length of  $25\text{ }\mu\text{m}$  and channel width of  $25\text{ }\mu\text{m}$ . The experimentally obtained results [8] are also shown.

The drain current ( $I_D$ ) versus the gate-to-source voltage ( $V_{GS}$ ) characteristics for different values of the body-to-source voltage ( $V_{BS}$ ) are shown in Figs.2.4 and 2.5 for the drain-to-source voltage  $V_{DS} = 0.5\text{ V}$  for two MOSFETs having channel lengths of  $0.55\text{ }\mu\text{m}$  and  $25\text{ }\mu\text{m}$  respectively. Also shown in these figure are the experimental results obtained by Joardar *et al.* [8]. Our simulated model results match well with the experimental results.

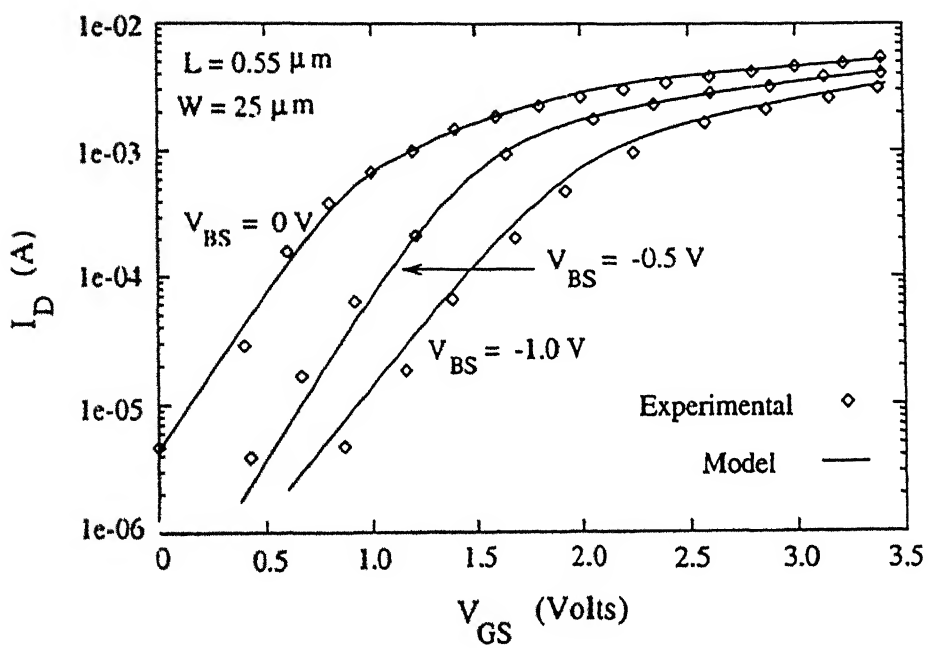


Figure 2.4:  $I_D$ - $V_{GS}$  characteristics obtained from our simulation for  $V_{DS} = 0.5\text{ V}$  and different values of  $V_{BS}$  for a MOSFET having channel length of  $0.55\text{ }\mu\text{m}$  and channel width of  $25\text{ }\mu\text{m}$ . The experimentally obtained results [8] are also shown for the sake of comparison.

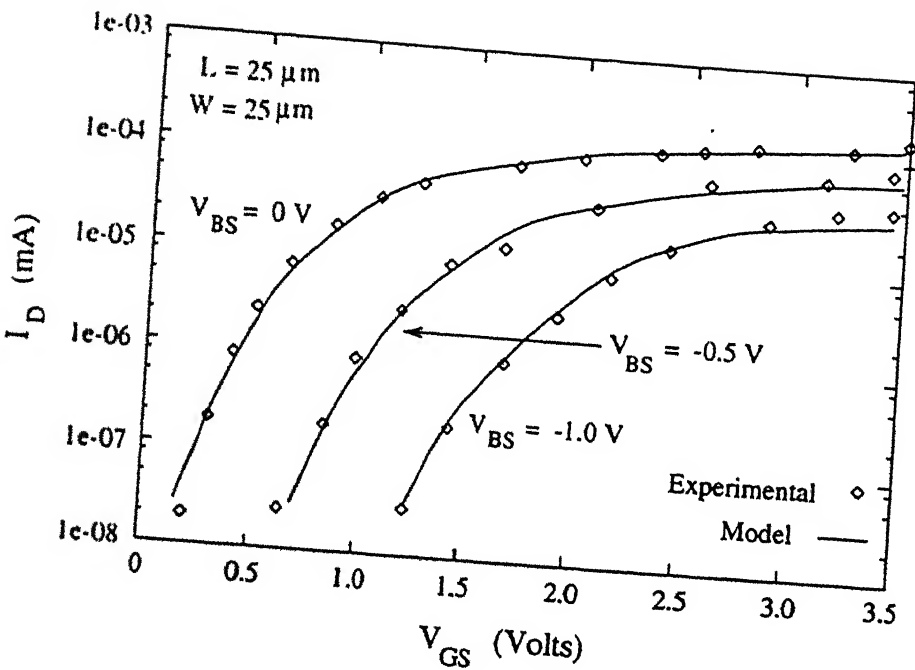


Figure 2.5:  $I_D$ - $V_{GS}$  characteristics obtained from our simulation for  $V_{DS} = 0.5\text{ V}$  and different values of  $V_{BS}$  for a MOSFET having channel length of  $25\text{ }\mu\text{m}$  and channel width of  $25\text{ }\mu\text{m}$ . The experimentally obtained results [8] are also shown for the sake of comparison.

The transconductance ( $g_m$ ) versus the gate-to-source voltage ( $V_{GS}$ ) characteristics are shown in Figs. 2.6 and 2.7 for the body-to-source voltage  $V_{BS} = 0\text{ V}$  and for the drain-to-source voltage  $V_{DS} = 0.5\text{ V}$ , for two MOSFETs having channel lengths of  $0.55\text{ }\mu\text{m}$  and  $25\text{ }\mu\text{m}$  respectively. The experimental results obtained from Joardar *et al.* [8] are also shown for the sake of comparison. Our simulated model results match well with the experimentally obtained results.

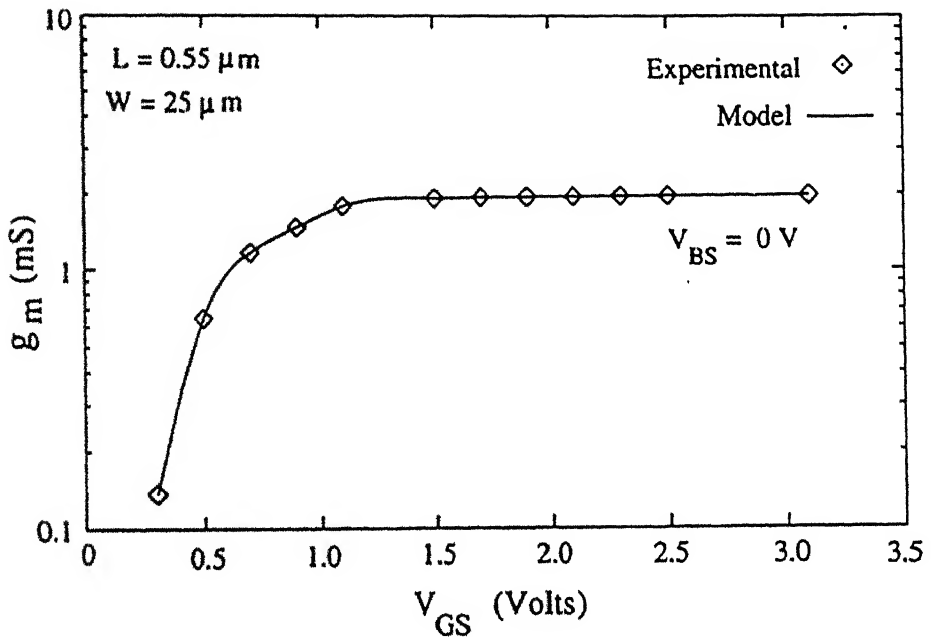


Figure 2.6:  $g_m$ - $V_{GS}$  characteristics obtained from our simulation for  $V_{BS} = 0 V$  and  $V_{DS} = 0.5 V$ , for a MOSFET having channel length of  $0.55 \mu m$  and channel width of  $25 \mu m$ . The experimentally obtained results [8] are also shown for the sake of comparison.

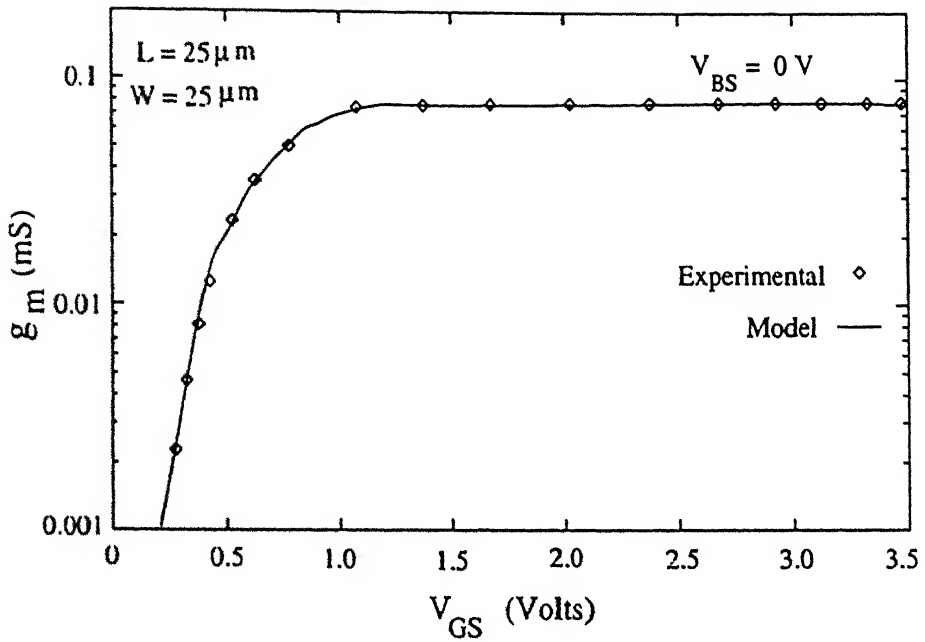


Figure 2.7:  $g_m$ - $V_{GS}$  characteristics obtained from our simulation for  $V_{BS} = 0$  V and  $V_{DS} = 0.5$  V, for a MOSFET having channel length of  $25 \mu\text{m}$  and channel width of  $25 \mu\text{m}$ . The experimentally obtained results [8] are also shown for the sake of comparison.

The output conductance ( $g_{ds}$ ) versus the drain-to-source voltage ( $V_{DS}$ ) characteristics for different values of the gate-to-source voltage ( $V_{GS}$ ) are shown in Figs.2.8 and 2.9 for the body-to-source voltage  $V_{BS} = 0$  V for two MOSFETs having channel lengths of  $0.55 \mu\text{m}$  and  $25 \mu\text{m}$  respectively. The experimental results reported by Joardar *et al.* [8] are also shown in the figure. Our model results match well with the experimental results, and no discontinuity is observed in the characteristics.

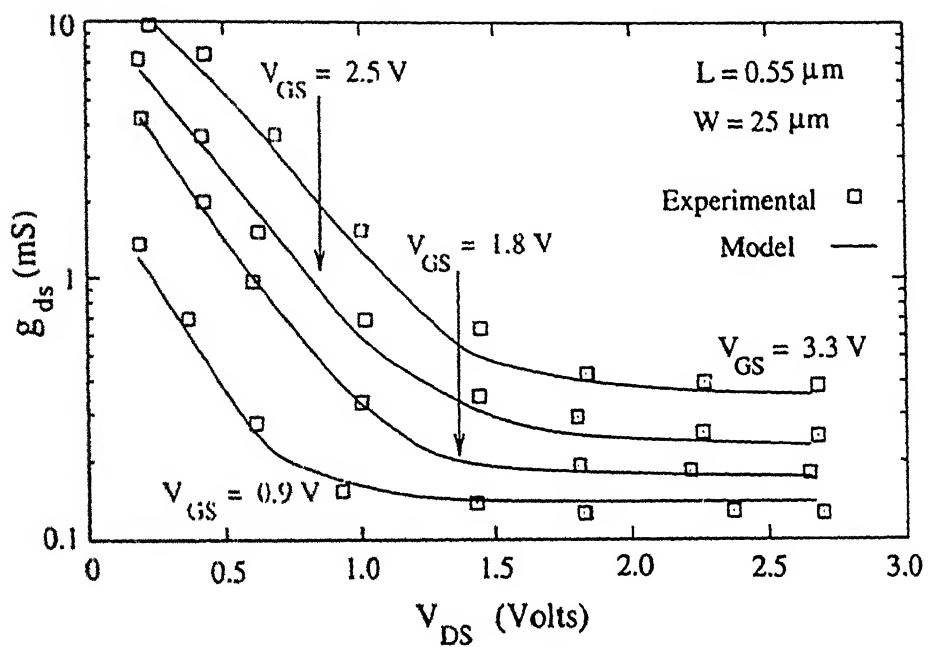


Figure 2.8:  $g_{ds}$ - $V_{DS}$  characteristics obtained from our simulation for different values of  $V_{GS}$  for  $V_{BS} = 0$  V for a MOSFET having channel length of  $0.55 \mu\text{m}$  and channel width of  $25 \mu\text{m}$ . The experimentally obtained results [8] are also shown for the sake of comparison.

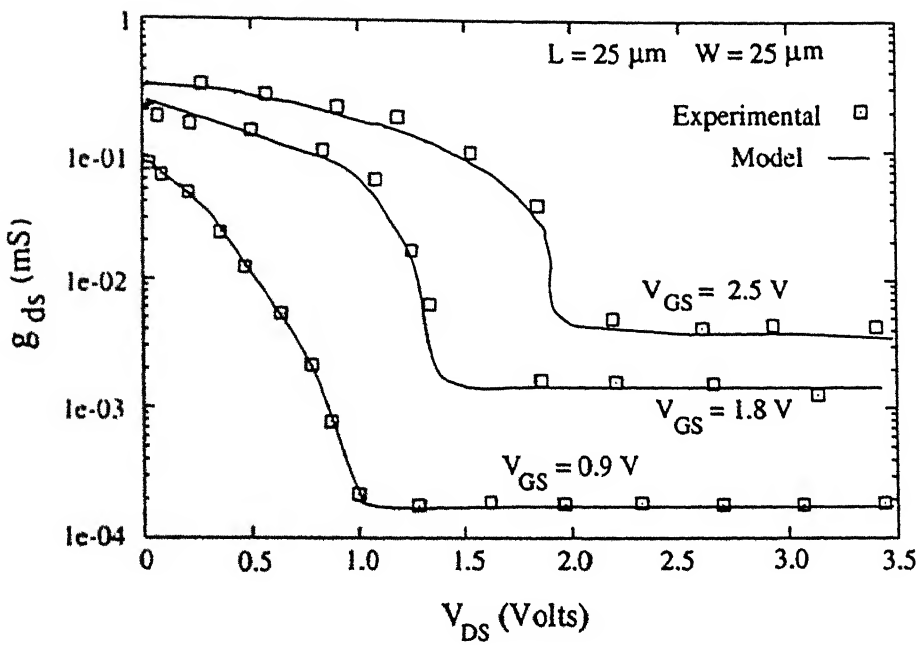


Figure 2.9:  $g_{ds}$ - $V_{DS}$  characteristics obtained from our simulation for different values of  $V_{GS}$  for  $V_{BS} = 0$  V for a MOSFET having channel length of  $25 \mu m$  and channel width of  $25 \mu m$ . The experimentally obtained results [8] are also shown and compared with our model results.

The MOSFET model developed by Joardar *et al.* was simulated and the measured as well as the simulated data are shown for a long channel and a short channel MOSFET. There is no discontinuity observed in the simulated drain current and conductance characteristics with respect to the terminal voltages. Also, a good match is obtained on comparison of model simulation results with the measured ones reported by Joardar *et al.* [8].

# Chapter 3

## The Substrate Current Model

### 3.1 Introduction

With ever decreasing device dimensions in order to achieve faster and denser MOSFET ICs, the importance of proper modeling of the substrate leakage current has grown manifold. When a MOSFET is biased in the saturation region, a measurable substrate current  $I_{sub}$  always flows. This current is the result of the electron-hole pair generation in the surface depletion region near the drain due to impact ionization. It is extremely sensitive to device dimensions, channel doping, terminal voltages, and temperature. Thus, there exists a need to accurately model the substrate current for proper circuit simulation.

Several analytical substrate current models have been developed and reported in literature [14-16]. The substrate current model proposed by Arora and Sharma [6] models the carrier ionization length  $l_d$  near the drain in a semi-empirical manner. Since the substrate current  $I_{sub}$  depends exponentially on

this ionization length  $l_d$ , a small error in its calculation can lead to a large error in the computed value of  $I_{sub}$ . As  $l_d$  is modeled semi-empirically, there is no physical significance for the model parameters,  $l_0$ ,  $l_1$ , and  $l_2$  appearing in [6].

In this work, a new physics based model for the ionization length  $l_d$  is proposed, along the lines adopted by Wong and Poon [7]. This model for  $l_d$  is then used in order to obtain an improved analytical expression for the substrate current  $I_{sub}$ .

### 3.2 Model Formulation

~~for~~

Consider the MOSFET structure in saturation, as shown in Fig.3.1, ~~Figure~~.  $t_{ox}$  represents the gate-oxide thickness,  $l_d$  is the length of the velocity saturation region (the impact ionization region),  $x_j$  is the drain junction depth,  $L$  is the effective channel length, and  $V_D$ ,  $V_G$ , and  $V_S$  represent the drain, gate, and source voltages respectively.

The substrate current  $I_{sub}$  in an n-channel MOSFET can be given by [6]

$$I_{sub} = I_D \int_{L-l_d}^L \alpha_n dy, \quad (3.1)$$

where  $I_D$  is the drain current, and  $\alpha_n$  is the impact ionization rate of the high energy carriers in  $[cm^{-1}]$  in the velocity saturated part of the channel (i.e.,  $l_d$ ).

The approximate expression for the impact ionization rate  $\alpha_n$  can be given by

$$\alpha_n = A_i e^{-B_i/E}, \quad (3.2)$$

where  $A_i$  and  $B_i$  are ionization constants in  $\text{cm}^{-1}$  and  $\text{V}/\text{cm}$  respectively. Therefore, the current expression [Eqn.(3.1)] can be rewritten as

$$I_{sub} = I_D A_i \int_{L-l_d}^L e^{-B_i/E(y)} dy. \quad (3.3)$$

For a MOS transistor operating in the saturation mode, the region near the drain is often called the velocity saturation region. The electric field in this region increases significantly and causes impact ionization due to high energy carriers traveling through this region. In order to obtain an expression for the electric field distribution  $E(y)$  in the channel, consider Fig.3.1.

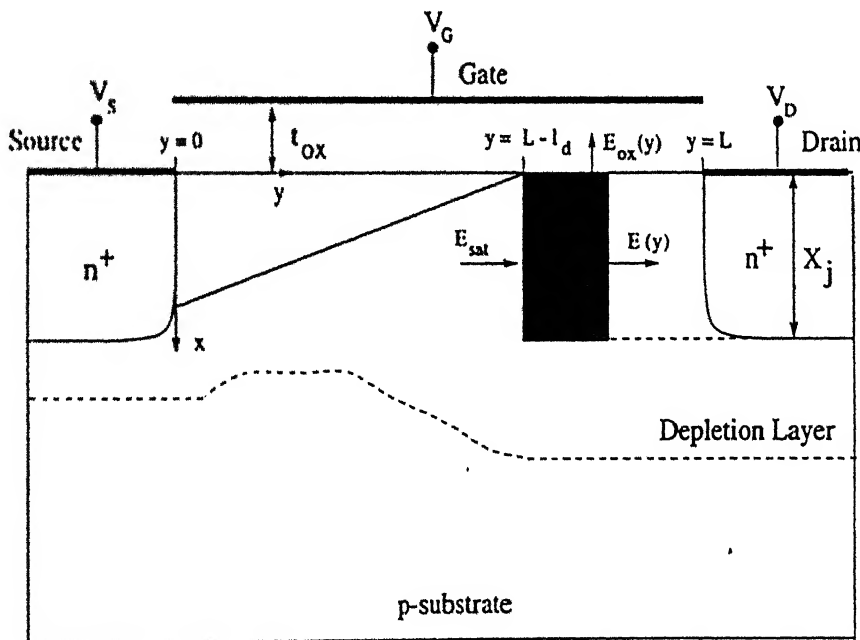


Figure 3.1: Figure showing the coordinate system, velocity saturation region, and boundary conditions, for evaluating the channel electric field  $E(y)$ .

Following the analyses reported by Sonoda *et al.* [17] and Wong and Poon [7], we apply Gauss' law to the shaded region in the velocity saturated part of the channel, as shown in Fig.3.1, in order to obtain the following expression [7]

$$-E_{sat}x_j + E(y)x_j + \frac{\epsilon_{ox}}{\epsilon_{Si}} \int_{L-l_d}^y E_{ox}(y) dy = \frac{qN_A}{\epsilon_{Si}} x_j (y - L + l_d), \quad (3.4)$$

where  $E_{ox}(y)$  is the electric field normal to the  $Si/SiO_2$  interface given by  $E_{ox}(y) = \frac{V_G - V_T - V(y)}{l_{ox}}$ ,  $V_T$  is the threshold voltage,  $V(y)$  is the potential along the channel,  $E_{sat}$  is the minimum electric field for velocity saturation, and  $N_A$  is the substrate doping density.

In Eqn.(3.4), the electric field flux flowing from the velocity saturation region to the substrate is assumed to be negligible. The electric field in the channel  $E(y)$  is assumed to be independent of the depth  $x$  [17], and it is assumed to vary linearly from zero (at  $y = 0$ ) to  $E_{sat}$  (at  $y = L - l_d$ ). Thus,  $dE(y)/dy$  at  $y = L - l_d$  can be approximated by [17]

$$\frac{dE(y)}{dy} \Big|_{y=L-l_d} = \frac{E_{sat}}{L - l_d}. \quad (3.5)$$

Using the boundary condition given by Eqn.(3.5), and following the approach similar to that adopted by Sonoda *et al.* [17], one gets the following equation for the channel potential  $V(y)$

$$V(y) = \frac{\lambda^2 E_{sat}}{L - l_d} (\cosh(D) - 1) + \lambda E_{sat} \sinh(D) + V_{Dsat}, \quad (3.6)$$

where  $V_{Dsat}$  is the drain saturation voltage at  $y = L - l_d$ ,  $D$  is equal to

$(y - L + l_d)/\lambda$ , and  $\lambda$ , the characteristic ionization length, is defined as [7]

$$\lambda = \sqrt{\frac{\epsilon_{Si}}{\epsilon_{ox}} x_j t_{ox}}. \quad (3.7)$$

Differentiating Eqn.(3.6) with respect to  $y$ , one obtains the expression for the electric field  $E(y)$ , given by

$$E(y) = \frac{\lambda E_{sat}}{L - l_d} \sinh(D) + E_{sat} \cosh(D). \quad (3.8)$$

From Eqns.(3.6) and (3.8) and using the identity  $\cosh^2(D) - \sinh^2(D) = 1$ , one gets the following relation for  $E(y)$

$$E(y) = \sqrt{\left(\frac{V(y) - V_{Dsat}}{\lambda} + \frac{\lambda E_{sat}}{L - l_d}\right)^2 + E_{sat}^2 - \frac{\lambda^2 E_{sat}^2}{(L - l_d)^2}}. \quad (3.9)$$

Differentiating Eqn.(3.9) with respect to  $y$ , one gets

$$dy = \frac{\lambda dE}{\sqrt{E(y)^2 + \frac{\lambda^2 E_{sat}^2}{(L - l_d)^2} - E_{sat}^2}}. \quad (3.10)$$

Changing the variable  $y$  in the expression for  $I_{sub}$  [Eqn.(3.3)] to  $E$  one obtains

$$I_{sub} = I_D A_i \lambda \int_{E_{sat}}^{E_m} \frac{e^{-B_i/E(y)}}{\sqrt{E(y)^2 - E_{sat}^2 + b^2}} dE, \quad (3.11)$$

where  $b$  is equal to  $\lambda E_{sat}/(L - l_d)$ ,  $E_{sat}$  is the electric field at  $y = L - l_d$ , and  $E_m$  is the maximum electric field at  $y = L$ .

The integral appearing in Eqn.(3.11) does not have a closed form solution. However, based on the assumption that  $E_m$  is much greater than  $E_{sat}$ , the expression for  $I_{sub}$  can be approximated as [6]

$$I_{sub} \approx I_D A_i \lambda \frac{1}{\sqrt{E_m^2 - E_{sat}^2 + b^2}} \cdot \frac{E_m^2}{B_i} e^{-B_i/E_m}. \quad (3.12)$$

In Eqn.(3.12), the term  $E_{sat}^2$  and  $b^2$  can be neglected as compared to  $E_m^2$ , and the simplified expression for  $I_{sub}$  can be given by

$$I_{sub} \approx I_D \frac{A_i}{B_i} \lambda E_m e^{-B_i/E_m}. \quad (3.13)$$

In this work, the maximum electric field  $E_m$  has been modeled empirically as

$$E_m \approx \frac{V_{DS} - \eta V_{Dsat}}{\beta l_d}, \quad (3.14)$$

where  $\eta$  and  $\beta$  are dimensionless fitting parameters. Thus, substituting the expression for  $E_m$  [Eqn.(3.14)] into the expression for  $I_{sub}$  [Eqn.(3.13)], a new analytical expression for the substrate current  $I_{sub}$  has been obtained in this work, which is given by

$$I_{sub} = I_D \frac{A_i}{B_i} (V_{DS} - \eta V_{Dsat}) \frac{\lambda}{\beta l_d} e^{-l_d \beta B_i / (V_{DS} - \eta V_{Dsat})}. \quad (3.15)$$

The ionization length  $l_d$  can be determined as a function of the channel length,  $\lambda$ , and  $V_D - V_{Dsat}$  [7]. In order to determine this relation, consider Eqn.(3.6), which gives the potential as a function of the position in the channel.

At  $y = L$ ,  $V(y)$  is equal to the drain voltage  $V_D$ . Substituting this in Eqn.(3.6), we get the following expression

$$\frac{V_D - V_{Dsat}}{\lambda E_{sat}} = \frac{\lambda}{L - l_d} (\cosh(\frac{l_d}{\lambda}) - 1) + \sinh(\frac{l_d}{\lambda}). \quad (3.16)$$

Substituting  $\lambda/(L - l_d)$  as  $a$ ,  $(V_D - V_{Dsat})/(\lambda E_{sat})$  as  $b$ , and  $e^{l_d/\lambda}$  as  $c$  in Eqn.(3.16), one obtains the following relation

$$2b = a(c + \frac{1}{c} - 2) + (c - \frac{1}{c}). \quad (3.17)$$

It is to be noted that all the three terms  $a$ ,  $b$ , and  $c$  depend on  $l_d$ . However, since the term  $c$  is exponentially dependent on  $l_d$ , hence, its variation with  $l_d$  would be much more drastic than the variations in the terms  $a$  and  $b$  with the variation in  $l_d$ . Therefore, Eqn.(3.17) is expressed as a quadratic equation in  $c$  and the solution can be given by

$$c = \frac{b + a + \sqrt{b^2 + 2ab + 1}}{a + 1}. \quad (3.18)$$

Thus, the ionization length  $l_d$  can be given by

$$l_d = \lambda \ln\left(\frac{b + a + \sqrt{b^2 + 2ab + 1}}{a + 1}\right). \quad (3.19)$$

In this work, an approximation is used for the term  $a$ , which is given by

$$a = \frac{\lambda}{L - l_d} \approx \frac{\lambda}{L - K\lambda}, \quad (3.20)$$

where  $K$  is a dimensionless model parameter which depends on  $V_D - V_{Dsat}$ . In this work,  $K$  has been modeled as

$$K = K_1(V_D - V_{Dsat})^2 + K_2(V_D - V_{Dsat}) + K_3, \quad (3.21)$$

where  $K_1$  ( $V^{-2}$ ),  $K_2$  ( $V^{-1}$ ), and  $K_3$  (dimensionless) are fitting parameters.

In the evaluation of the substrate current  $I_{sub}$ ,  $V_{Dsat}$  is an important parameter which must be determined. It can be modeled as [6]

$$V_{Dsat} = LE_{sat}(\sqrt{1 + \frac{2(V_{GS} - V_T)}{\alpha LE_{sat}}} - 1), \quad (3.22)$$

where  $\alpha$  is a fitting parameter.

The improved model developed for  $I_{sub}$  in this section was simulated and the results obtained were compared with the experimental data given in [6]. The results are presented in the next section.

### 3.3 Analysis and results

For the calculation of the values of the substrate current  $I_{sub}$  as a function of  $V_{GS}$ , the parameters required to be extracted are  $A_i$ ,  $B_i$ ,  $\eta$ ,  $\lambda$ ,  $l_d$ ,  $\beta$ , and  $\alpha$  [Eqn.(3.15)]. The device parameters used for the simulation are  $x_j = 0.4 \mu m$  and  $t_{ox} = 150 A^\circ$ , which gives the value of  $\lambda$  to be equal to  $1.37 \mu m$  [from Eqn.(3.7)].

In this work, the simulated results obtained from the model developed for the ionization length  $l_d$  [Eqn.(3.19)] are plotted as a function of  $V_D - V_{Dsat}$

in Fig.3.2. The symbols in Fig.3.2 are the data generated from MINIMOS, obtained from Wong and Poon [7], for the channel length  $L = 0.5 \mu m$ . From a comparison of the two, the values of the fitting parameters  $K_1$ ,  $K_2$ , and  $K_3$  are obtained as  $-0.03 V^{-2}$ ,  $0.27 V^{-1}$ , and  $1.2$  respectively.

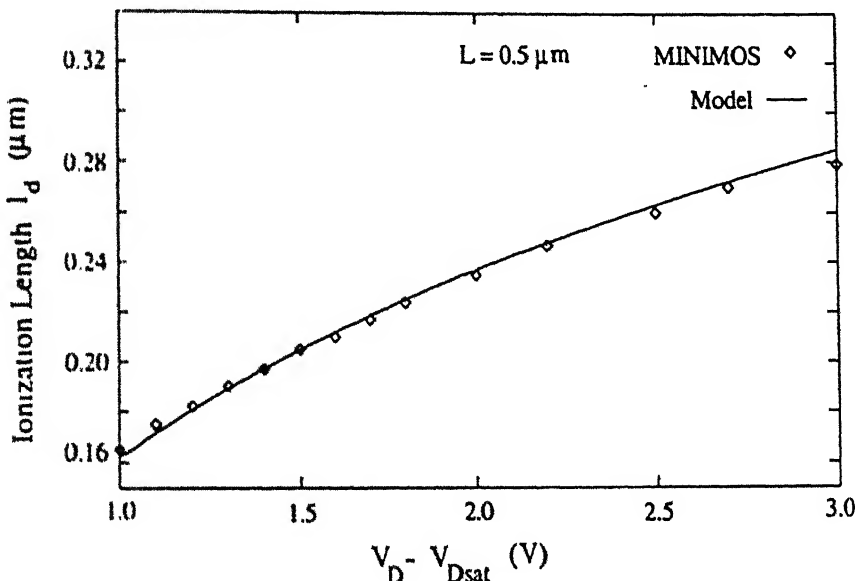


Figure 3.2: Ionization length  $l_d$  as a function of  $V_D - V_{Dsat}$ , for  $L = 0.5 \mu m$ . Symbols indicate MINIMOS generated data [7].

The values of the ionization length  $l_d$  obtained from Eqn.(3.19) are also plotted as a function of the channel length  $L$  in Fig.3.3, for  $V_D - V_{Dsat} = 2.0 V$  and  $2.5 V$ . The data generated from MINIMOS [7] are also shown in the figure. The results show a good match between the two.

The values of the fitting parameters  $K_1$ ,  $K_2$ , and  $K_3$  extracted above are used to determine the ionization length  $l_d$ . The values of the ionization constants  $A_i$  and  $B_i$  are kept equal to  $2.54 \times 10^6 cm^{-1}$  and  $1.92 \times 10^6 V/cm$  respectively, and those of the saturation electric field  $E_{sat}$  and  $\alpha$  are kept equal to  $1.053 \times 10^4 V/cm$  and  $1.19$  respectively, as given by Arora and Sharma [6].

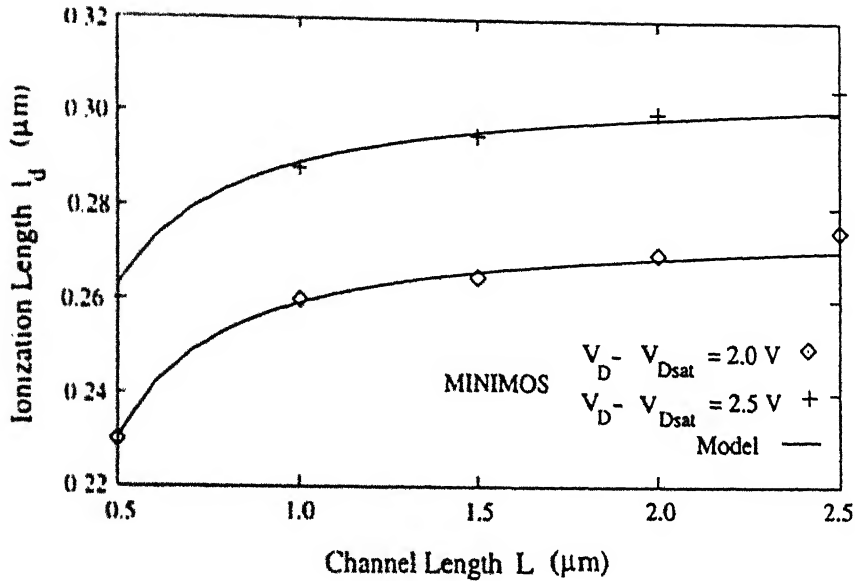


Figure 3.3: Ionization length  $l_d$  as a function of the channel length  $L$ , for  $V_D - V_{Dsat} = 2.0 \text{ V}$  and  $2.5 \text{ V}$ . Symbols indicate MINIMOS generated data [7].

In order to extract the values of the fitting parameters  $\beta$  and  $\eta$  used in our empirical expression for the maximum electric field  $E_m$  [Eqn.(3.14)], the exact equation for  $I_{sub}$  [Eqn.(3.11)] is integrated numerically and the results are plotted in Fig.3.4 as a function of  $V_{GS}$ . Then, the values obtained from the approximate equation for  $I_{sub}$  [Eqn.(3.15)] are mapped onto it, and are also shown in Fig.3.4. From this mapping, the values of  $\beta$  and  $\eta$  are obtained. Table 3.1 shows the values of the extracted parameters needed for determining the substrate current  $I_{sub}$ .

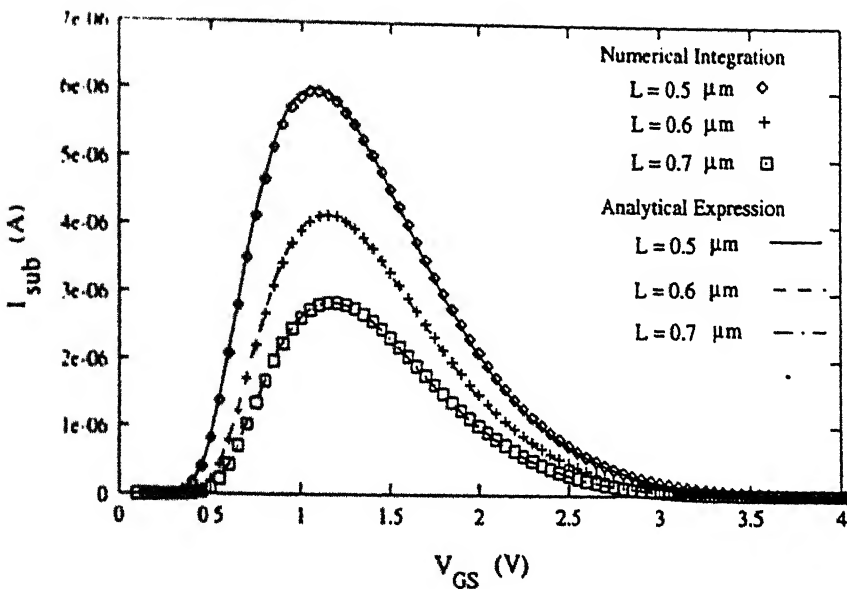


Figure 3.4: The values of  $I_{sub}$  obtained from the approximate relation [Eqn.(3.15)], and the numerically integrated values obtained from the exact expression [Eqn.(3.11)] versus the gate-to-source voltage  $V_{GS}$ , for three different channel lengths ( $0.5 \mu m$ ,  $0.6 \mu m$ , and  $0.7 \mu m$ ).

Table 3.1: The values of the parameters needed for determining the substrate current  $I_{sub}$ .

$A_i$ $10^6 (cm^{-1})$	$B_i$ $10^6 (V/cm)$	$E_{sat}$ $10^4 (V/cm)$	$\eta$	$\alpha$	$\beta$
2.54	1.92	1.053	1.32	1.19	0.244

The simulated results obtained from the analytical model equation for  $I_{sub}$  [Eqn.(3.15)], using the values of the model parameters extracted earlier, is

compared with the experimental data given by Arora and Sharma [6]. Figure 3.5 shows the substrate current  $I_{sub}$  obtained from our model as a function of the gate-to-source voltage  $V_{GS}$  for  $V_{DS} = 4.6 V$  and  $V_{BS} = 0 V$ . The experimental data reported by Arora and Sharma [6] is also shown for comparison. Our model results match well with the reported experimental results.

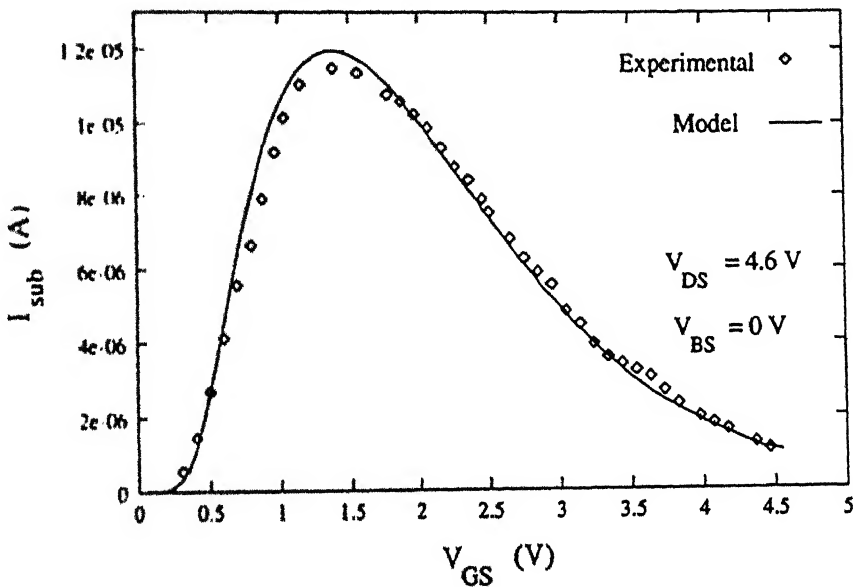


Figure 3.5: The simulated values of the substrate current  $I_{sub}$  obtained from our model as a function of the gate-to-source voltage  $V_{GS}$ , for  $V_{DS} = 4.6 V$  and  $V_{BS} = 0 V$ . The experimental data reported by Arora and Sharma [6] are also shown for comparison.

The nature of the substrate current is such that it initially increases with increasing  $V_{GS}$  and then it decreases as  $V_{GS}$  increases beyond a certain value, thus showing a peak at a particular value of  $V_{GS}$ . This can be physically explained as follows.

The substrate current  $I_{sub}$  is a function of  $I_{DS}$ ,  $V_{DS} - V_{Dsat}$ , and  $l_d$  [Eqn.(3.15)].

Initially, for a small  $V_{GS}$ ,  $I_{DS}$  increases rapidly with increasing  $V_{GS}$ , thus  $I_{sub}$  increases accordingly. However, as  $V_{GS}$  increases,  $V_{DS} - V_{Dsat}$  and  $l_d$  both decrease. Hence, a point is reached when the effect of increasing  $I_{sub}$  due to increasing  $V_{GS}$  is nullified by the decrease in  $I_{sub}$  due to the decreasing  $V_{DS} - V_{Dsat}$  and  $l_d$ . Then onwards  $I_{sub}$  decreases as  $V_{GS}$  is increased.

A simple and accurate approximation of the ionization length  $l_d$ , based on the calculation of the electric field distribution near the drain region has been developed in this work. Our model results are verified with the MINIMOS simulation results reported by Wong and Poon [7], and a good correlation between the two is obtained.

This new model for  $l_d$  is then used to calculate the substrate current. The results obtained from the improved substrate current model are then compared with the experimental data reported by Arora and Sharma [6], and a good match is obtained between the two.

# Chapter 4

## Transconductance Overshoot Model for Submicron MOSFETs

### 4.1 Introduction

Different analytical submicron MOSFET models have been developed in order to incorporate the various short channel effects. Most of these models accurately reproduce electrical characteristics of short channel devices down to half micron channel lengths. However, they encounter some difficulties in accurately reproducing electrical properties for devices with channel lengths less than  $0.1 \mu m$ .

One such effect that becomes predominant when device dimensions shrink is the electron *velocity overshoot*. It is one of the most important effects from the practical point of view, as it is directly related to the increase in the current drive and the transconductance of the device, which have been experimentally

observed in short channel MOSFETs. Some authors [1-4] have shown that the experimentally measured values for the transconductance for submicron MOSFETs (for channel lengths less than  $0.15 \mu m$ ) are higher than the theoretically predicted maximum values that can be reached.

Figures 4.1 and 4.2 show the drift velocity of the electrons as a function of time and distance from the source respectively in silicon for different values of the electric field [18]. From these two figures, it can be seen that for electric fields greater than  $10 \text{ kV/cm}$ , there is a possibility of velocity overshoot for electrons if the channel lengths are short enough.

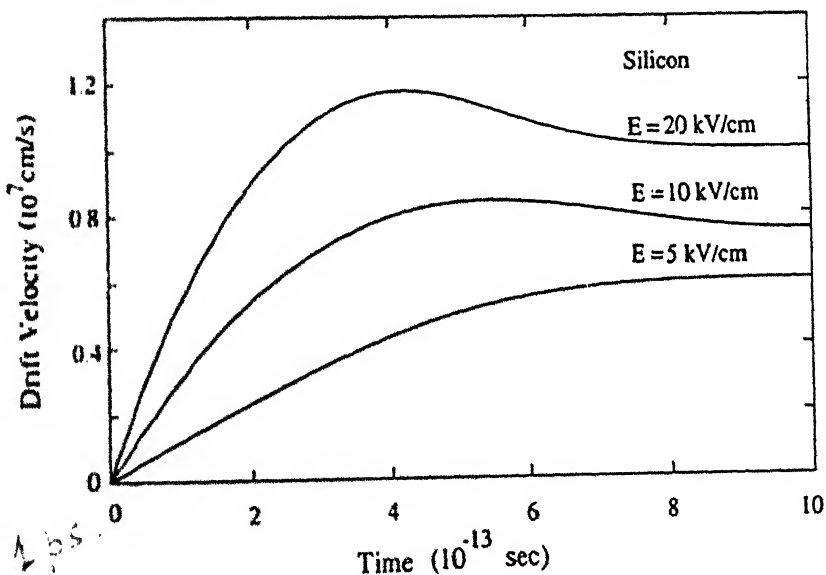


Figure 4.1: Variation of the drift velocity of electrons with time, for different values of the electric field  $E$  [18].

The principal aim of this work is to develop a model for the transconductance overshoot observed in ultra-short channel MOSFETs. In this work, the carriers under consideration are electrons. The MOSFET transconductance ( $g_m$ ) is the most important figure of merit when dealing with large signal

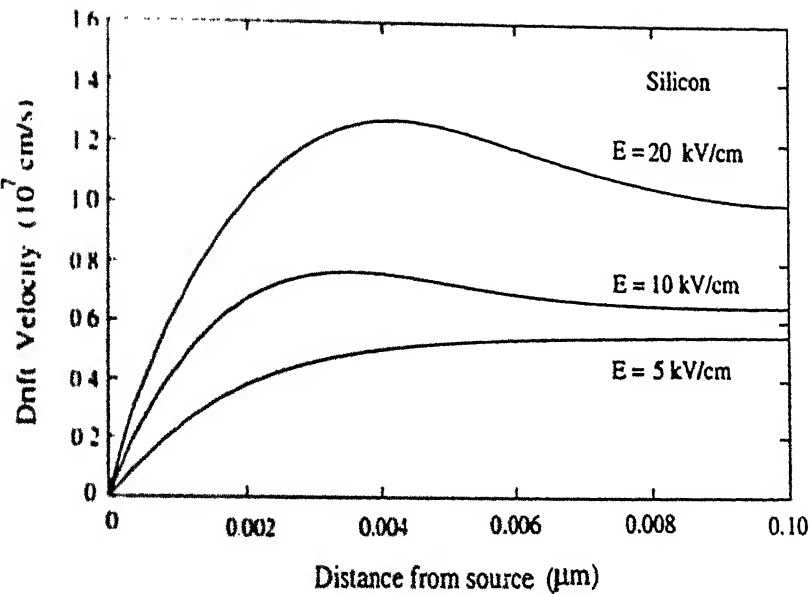


Figure 4.2: Variation of the drift velocity of electrons as a function of distance from the source for different values of the electric field  $E$  [18].

switching performance of logic devices, as the time constant for MOSFETs to charge a load capacitance  $C$  is proportional to  $C/g_m$ . This parameter is also of immense importance from the analog circuit point of view, since the gain of the MOSFET amplifiers is directly proportional to  $g_m$ .

Many models have been developed and presented in literature, which incorporate the carrier velocity overshoot effects [5,19,20]. The drift velocity  $v$  of electrons in an inhomogeneous electric field has been expressed as [5,21]

$$v = v_{\text{th}} + \lambda \frac{dE}{dx}, \quad (4.1)$$

where  $\lambda$  is the parameter proposed by Thorner [21], which depends on the longitudinal electric field,  $v_{\text{th}}$  is the drift velocity in a homogeneous field, and  $E$  is the electric field in the channel. The corresponding drain current expression

is given by [5]

$$I_D = \frac{W\mu_0 F(V_{GS}, V_{DS})}{L(1 + \frac{\mu_0 V_{DS}}{v_{sat} L})} + \lambda_a \frac{W}{L^2} F(V_{GS}, V_{DS}), \quad (4.2)$$

where  $\lambda_a$  is the velocity overshoot parameter ( $cm^3/V\text{-sec}$ ) as given by Roldan *et al* [5],  $\mu_0$  is the low-field electron mobility,  $v_{sat}$  is the saturation velocity of electrons,  $W$  is the channel width,  $L$  is the channel length, and

$$F(V_{GS}, V_{DS}) = \int_0^{V_{DS}} Q'(V) dV \quad (4.3)$$

where  $Q'(V)$  is the mobile channel charge per unit area.

From Eqn.(4.2), the MOSFET transconductance  $g_m$  can be given as [5]

$$g_m = \frac{W}{L} \frac{\partial F(V_{GS}, V_{DS})}{\partial V_{GS}} \left[ \frac{\mu_0}{1 + \frac{\mu_0 V_{DS}}{v_{sat} L}} + \frac{\lambda_a}{L} \right]. \quad (4.4)$$

This expression assumes that the low-field mobility  $\mu_0$  is not a function of the applied gate-to-source voltage  $V_{GS}$ . This is contrary to the conventional mobility model [11], which accounts for the dependence of mobility on  $V_{GS}$ , given by

$$\mu_G = \frac{\mu_0}{1 + \theta(V_{GS} - V_T)}, \quad (4.5)$$

where  $\mu_G$  is the mobility as a function of the gate-to-source voltage  $V_{GS}$ ,  $V_T$  is the threshold voltage,  $\theta$  is the mobility degradation coefficient [11], and  $\mu_0$  is the low field mobility at  $V_{GS} = V_T$ . Tsividis [11] has given the empirical

expression for  $\theta$  as

$$\theta = \frac{\beta_\theta}{t_{ox}}, \quad (4.6)$$

where the parameter  $\beta_\theta$  typically varies from 0.001 to 0.004  $\mu m/V$  [11], and  $t_{ox}$  is the oxide thickness. Also, the parameter  $\lambda_a$  has been shown to be functions of the low-field mobility and the temperature [5], however, the dependence of this parameter on the bias voltage is not shown.

The aim of this work is to develop an analytical mobility model in order to explain the phenomenon of higher than theoretically predicted transconductance observed for ultra-short channel length MOSFETs.

## 4.2 Model Formulation

Assume that the source is located at  $x = 0$  and the potential at that point is zero. The drain is assumed to be at  $x = L$  (where  $L$  is the effective channel length) and is at a potential  $V_{DS}$ . The drain current  $I_D$  can be calculated as a product of the mobile channel charge per unit area, the channel width, and the electron velocity, i.e., the electrons in transit model, given by

$$I_D = Q'(V)vW. \quad (4.7)$$

The drift velocity model used in this work is given by [5]

$$v = \frac{\mu E}{1 + \frac{E}{E_C}}, \quad (4.8)$$

where  $E$  is the electric field in the channel,  $E_C$  is the critical electric field for velocity saturation, and  $\mu$  is the enhanced electron mobility, a model for which is proposed later in this chapter. This drift velocity model predicts an almost linear increase of the velocity  $v$  with the electric field  $E$  until the critical electric field  $E_C$  is reached, beyond which the velocity saturates to the saturation velocity  $v_{sat}$ . This behavior of the carrier velocity  $v$  as a function of the electric field  $E$  is shown in Fig.4.3. For getting the characteristics of Fig.4.3, the values of  $E_C$  and  $v_{sat}$ , which are substituted in Eqn.(4.8), are assumed to be equal to  $25 \text{ kV/cm}$  and  $10^7 \text{ cm/s}$  respectively. Also, an approximate expression for  $E_C$  can be given as  $E_C = v_{sat}/\mu_G$ , where  $\mu_G$  is the mobility given by Eqn.(4.5).

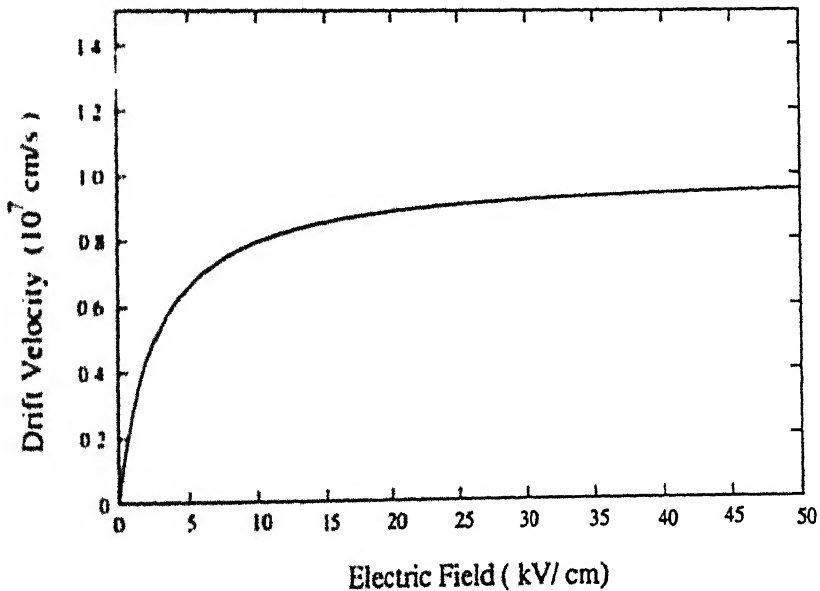


Figure 4.3: Variation of the drift velocity of electrons with the electric field. The values used are  $E_C = 25 \text{ kV/cm}$  and  $v_{sat} = 10^7 \text{ cm/s}$ . For low fields,  $v \approx \mu E$  and for high fields,  $v \approx v_{sat}$ .

In this work, we propose a new model for the mobility as follows. The

origin of the proposed equation is semi-empirical. Physically, it is obvious that the mobility would increase with larger applied drain-to-source voltage  $V_{DS}$  and smaller channel length  $L$ . However, at the same time, it is a function of the critical electric field  $E_C$ . Thus, the proposed model is given as

$$\mu = \mu_G \left(1 + \frac{L_{co} V_{DS}}{E_{co} L^2}\right), \quad (4.9)$$

where  $\mu_G$  is mobility as given in Eqn.(4.5), and  $L_{co}$  and  $E_{co}$  are empirical model parameters. Substituting Eqns.(4.8) and (4.9) in Eqn.(4.7), we get

$$I_D = WQ'(V) \frac{\mu_G \left(1 + \frac{L_{co} V_{DS}}{E_{co} L^2}\right)}{1 + \frac{\mu_G E}{v_{sat}}} E. \quad (4.10)$$

Rearranging terms, we get

$$I_D \left(1 + \frac{\mu_G E}{v_{sat}}\right) dx = WQ'(V) \mu_G \left(1 + \frac{L_{co} V_{DS}}{E_{co} L^2}\right) dV. \quad (4.11)$$

In the term  $[1 + (\mu_G E / v_{sat})]$  in Eqn.(4.10), the electric field  $E$  can be assumed to have a constant value, which is equal to  $V_{DS}/L$ . This assumption is valid since as  $E$  changes, there is only a slight variation in the term  $[1 + (\mu_G E / v_{sat})]$  as, in general,  $\mu_G E / v_{sat} \ll 1$ . Substituting  $E = V_{DS}/L$  and integrating the left-hand side of Eqn.(4.11) from 0 to  $L$  and the right-hand side from 0 to  $V_{DS}$ , in a manner similar to that adopted by Roldan et al. [5], we get

$$\int_0^L I_D \left(1 + \frac{\mu_G V_{DS}}{v_{sat} L}\right) dx = \int_0^{V_{DS}} WQ'(V) \mu_G \left(1 + \frac{L_{co} V_{DS}}{E_{co} L^2}\right) dV, \quad (4.12)$$

or

$$I_D = \frac{W}{L} \frac{\mu_G (1 + \frac{L_{co}}{E_{co}} \frac{V_{DS}}{L^2}) F(V_{GS}, V_{DS})}{1 + \frac{\mu_G V_{DS}}{v_{sat} L}}. \quad (4.13)$$

Equation (4.13) gives the expression for the drain current, which was derived using the new model for the mobility proposed in this work. The transconductance can be obtained by taking the derivative of Eqn.(4.13) with respect to  $V_{GS}$ , which can be given by

$$g_m = \frac{W}{L} (1 + \frac{L_{co}}{E_{co}} \frac{V_{DS}}{L^2}) A, \quad (4.14)$$

where

$$A = \frac{(\partial F / \partial V_{GS}) \mu_G + F(d\mu_G / dV_{GS})}{1 + \frac{\mu_G V_{DS}}{v_{sat} L}} - \frac{[F \mu_G V_{DS} / (v_{sat} L)] (d\mu_G / dV_{GS})}{(1 + \frac{\mu_G V_{DS}}{v_{sat} L})^2}, \quad (4.15)$$

which can be expressed as

$$A = \frac{(\partial F / \partial V_{GS}) \mu_G}{1 + \frac{\mu_G V_{DS}}{v_{sat} L}} \left( 1 + \frac{\beta}{1 + \frac{\mu_G V_{DS}}{v_{sat} L}} \right), \quad (4.16)$$

where  $\beta$  is given by

$$\beta = \frac{F(\partial \mu_G / \partial V_{GS})}{(\partial F / \partial V_{GS}) \mu_G} \quad (4.17)$$

Differentiating the expression for  $\mu_G$  [Eqn.(4.5)] with respect to  $V_{GS}$ , we get

$$\frac{d\mu_G}{dV_{GS}} = \frac{-\mu_0 \theta}{[1 + \theta(V_{GS} - V_T)]^2}. \quad (4.18)$$

Substituting Eqn (4.16) in Eqn.(4.14), we get the final expression for the transconductance as

$$g_m = \frac{W}{L} \left(1 + \frac{L_{co} V_{DS}}{E_{co} L^2}\right) \frac{(\partial F/\partial V_{GS})\mu_G}{1 + \frac{\mu_G V_{DS}}{v_{sat} L}} \left(1 + \frac{\beta}{1 + \frac{\mu_G V_{DS}}{v_{sat} L}}\right). \quad (4.19)$$

Equation (4.19) is the expression for the MOSFET transconductance, which incorporates the improved mobility model proposed in this work. The transconductance overshoot factor  $F_v$  can be given as

$$F_v = 1 + \frac{L_{co} V_{DS}}{E_{co} L^2}, \quad (4.20)$$

which is obviously greater than unity, and, in turn, predicts a higher than expected transconductance.

### 4.3 Results and Discussion

The simulated values of the transconductance obtained from Eqn.(4.19) are compared with the experimental values for a MOSFET reported by Sai-Halasz *et al.* [1] as a function of the channel length. This comparison is shown in Fig.4.4, which shows the transconductance per channel width ( $g_m/W$ ) as a function of the channel length  $L$  for two different temperatures (77 K and 300 K). In the figure, the experimental values [1] are denoted by symbols. From Fig.4.4, it can be seen that as the channel length decreases, there is a sharp increase in the transconductance. Our analytical model results match quite well with the experimental values reported by Sai-Halasz *et al.* [1]. The value of the parameter  $\partial F/\partial V_{GS}$  is kept the same as that given by Roldan *et al.* [5] and is given in Table 4.1.

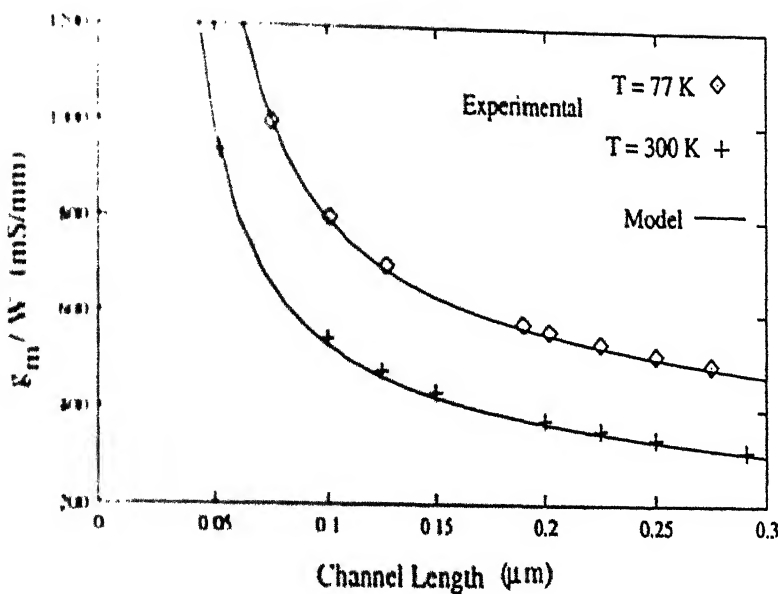


Figure 4.4 The transconductance per channel width reported by Sai-Halasz *et al.* [1] as a function of the channel length for two different temperatures (77 K and 300 K) are shown by symbols. The results simulated from our model (lines) are also shown for comparison. The parameter values used in the simulation are  $V_{GS} - V_T = 0.6$  V,  $V_{DS} = 0.8$  V, and  $t_{ox} = 4.5$  nm. The other model parameter values are shown in Table 4.1.

In the calculation for the transconductance  $g_m$ , the value for the low-field mobility  $\mu_0$  is assumed to be  $390 \text{ cm}^2/\text{V}\cdot\text{sec}$  and  $720 \text{ cm}^2/\text{V}\cdot\text{sec}$  for  $T = 300$  K and 77 K respectively [5]. The value of  $\beta_\theta$  [appearing in Eqn.(4.6)] is chosen to be equal to  $0.002 \mu\text{m}/\text{V}$ , and the value of the parameter  $\theta$  can be obtained from Eqn.(4.6) for a given value of  $t_{ox}$ . The values of  $\mu_0$  and  $\theta$  are then substituted in Eqn(4.5) in order to obtain the value for  $\mu_G$ . The critical electric field  $E_C$  is then computed from the expression  $E_C = v_{sat}/\mu_G$ .

The model parameters used in the expression for the transconductance [Eqn (4.19)] are  $L_{ox}$ ,  $E_{cr}$ ,  $\theta$ , and  $\beta$ . In this work, the values of the parameter

$E_{co}$  is taken to be equal to that of the critical electric field  $E_C$ . This can be justified as follows. The increase in the transconductance is observed only for high electric fields, i.e., for  $E > E_C$ . In our model, the drift velocity saturates for  $E$  greater than  $E_C$ . Therefore, in order to account for an increase in the transconductance, the mobility must increase [Eqn.(4.19)]. This is accomplished by keeping the parameter  $E_{co}$  to be equal to  $E_C$ . The values for the other two fitting parameters  $L_{co}$  and  $\beta$  are extracted from a match of the experimental and the simulated transconductance values. The extracted parameter values for this case are shown in Table 4.1.

Table 4.1: Extracted model parameter values obtained from a comparison of the results simulated from our model with experimental transconductance values reported by Sai-Halasz *et al.* [1].

Temp. (K)	$\mu_0$ ( $cm^2/V\text{-sec}$ )	$\mu_G$ ( $cm^2/V\text{-sec}$ )	$E_{co}$ (kV/cm)	$L_{co}$ ( $10^{-6}$ cm)	$\beta$	$v_{sat}$ ( $10^7$ cm/s)	$\partial F/\partial V_{GS}$ ( $10^{-7}$ C/ $cm^2$ )
300	390	307.9	25.98	0.935	0.48	0.8	5.2
77	720	568.4	17.59	0.791	0.48	1.0	5.5

The results obtained from our model are also compared with the ones reported by Pinto *et al.* [22]. The intrinsic transconductance versus channel length data given by Pinto *et al.* [22] were calculated by using accurate simulators which included the velocity overshoot effect. The simulator PADRE, used by Pinto *et al.* [22], made use of the energy transport equations [23-25], defined in terms of the average carrier drift velocities and temperature.

Figure 4.5 shows the transconductance per channel width  $g_m/W$  obtained

from our model, as a function of the channel length  $L$ , for different values for the low-field mobility ( $125, 250$ , and  $500 \text{ cm}^2/\text{V}\cdot\text{sec}$ ) at  $T = 300 \text{ K}$ . The results reported by Pinto *et al.* [22] are also shown in the same figure for the sake of comparison. The parameter values are extracted after matching our model results with the simulated transconductance values reported by Pinto *et al.* [22], and are shown in Table 4.2.

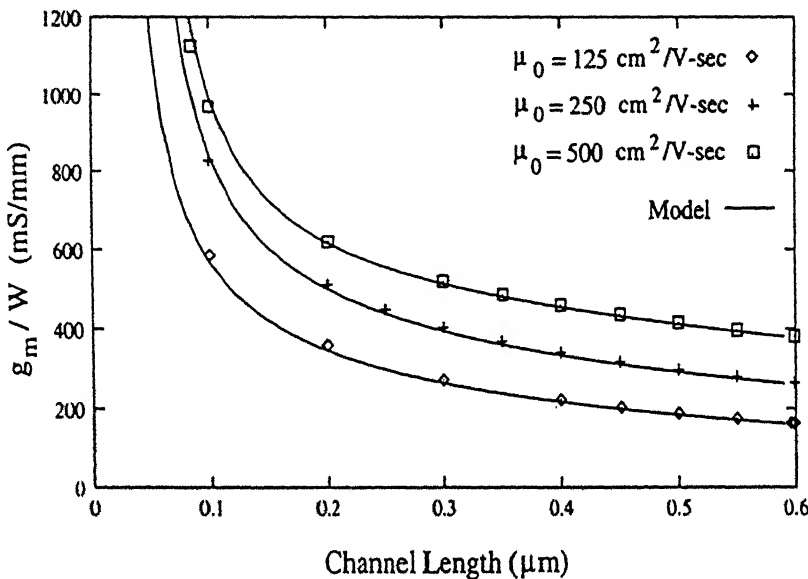


Figure 4.5: The simulated intrinsic transconductance per channel width reported by Pinto *et al.* [22] as a function of the channel length for three different values for the low-field mobility ( $125, 250$ , and  $500 \text{ cm}^2/\text{V}\cdot\text{sec}$ ) at  $T = 300 \text{ K}$ , shown by symbols. The results simulated from our model (lines) are also shown for comparison. The parameter values used in the simulation are  $V_{GS} = V_{DS} = 1.5 \text{ V}$ ,  $v_{sat} = 10^7 \text{ cm/s}$ ,  $\partial F(V_{GS}, V_{DS})/\partial V_{GS} = 10^{-6} \text{ C/cm}^2$ ,  $t_{ox} = 4 \text{ nm}$ , and  $V_T \approx 0.45 \text{ V}$ . The other parameter values are shown in Table 4.2.

Table 4.2: Extracted parameter values after comparison of our results with the simulated transconductance values reported by Pinto *et al.* [22].

$\mu_0$ ( $cm^2/V\text{-sec}$ )	$\mu_G$ ( $cm^2/V\text{-sec}$ )	$E_{co}$ ( $kV/cm$ )	$L_{co}$ ( $10^{-6} cm$ )	$\beta$
125	81.96	122	2.44	0.48
250	163.9	61	2.26	0.48
500	327.85	30.5	1.34	0.48

The transconductance overshoot factor  $F_v$  computed from Eqn.(4.20) is plotted as a function of the channel length for two different temperatures (77 K and 300 K) in Fig.4.6 along with the experimentally reported values by Sai-Halasz *et al.* [1]. It can be seen from the figure that for large channel lengths, the value of the overshoot factor  $F_v$  is close to unity, indicating that there is no increase in the transconductance. However, for channel lengths less than  $0.15 \mu m$ , the overshoot factor becomes quite significant. Our model parameter values are extracted after matching Eqn.(4.20) with the experimental values reported by Sai-Halasz *et al.* [1], and are presented in Table 4.3.

Table 4.3: Extracted model parameter values after comparison of the overshoot factor simulated from our model with the reported values by Sai-Halasz *et al.* [1].

Temp. (K)	$E_{co}$ ( $kV/cm$ )	$L_{co}$ ( $10^{-6} cm$ )
77	0.791	17.59
300	0.935	25.98

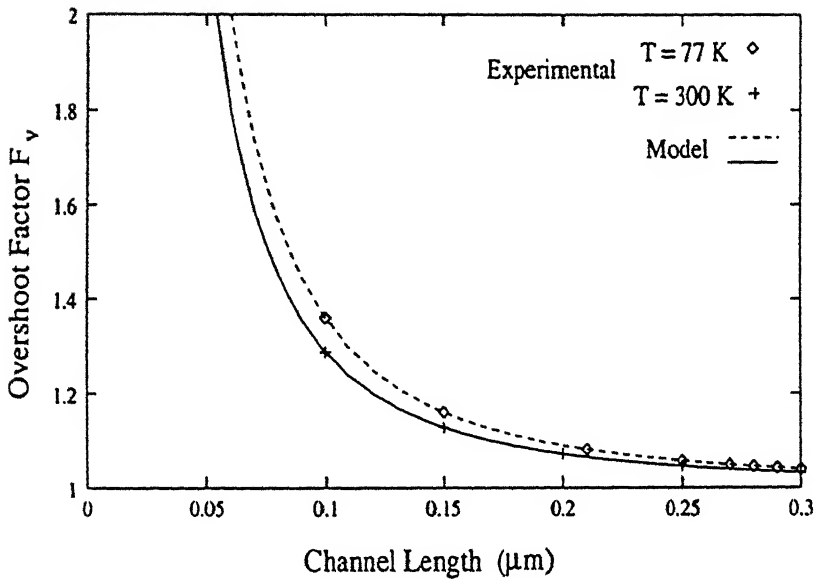


Figure 4.6: The room temperature (300 K) and low temperature (77 K) overshoot factor  $F_v$  as a function of the channel length, as reported by Sai-Halasz *et al.* [1], shown by symbols. The results simulated from our model (lines) are also shown for comparison. The parameter values used in the simulation are  $V_{GS} - V_T = 0.6 \text{ V}$  and  $V_{DS} = 0.8 \text{ V}$ . The other parameter values are given in Table 4.3.

The results obtained from our analytical transconductance model match well with the experimental data reported by Sai-Halasz *et al.* [1], as well as with the simulated transconductance behavior reported by Pinto *et al.* [22]. It has been observed in this work that the values of the model parameter  $L_{co}$  change with the low-field mobility  $\mu_0$ , and, hence, also with  $\mu_G$ . Table 4.4 shows the variation of this parameter with  $\mu_G$ .

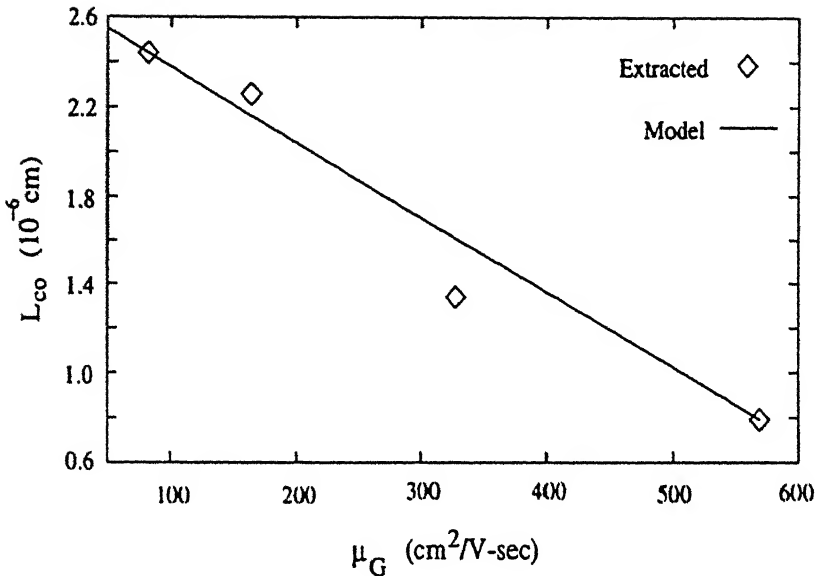


Figure 4.7: Extracted values of the parameter  $L_{co}$  (shown by symbols) as a function of the mobility  $\mu_G$  along with a straight line best fit.

model the variation of the mobility itself with the channel electric field. This mobility is also a function of the drain-to-source voltage, oxide thickness, gate-to-source voltage, and channel length. With large channel electric field and small channel length, the mobility is bound to increase, and the increase in the transconductance is then accounted for by the correspondingly enhanced electron mobility.

Equation (4.20), which gives the expression for the overshoot component of the transconductance, is seen to be inversely proportional to the channel length and directly proportional to the electric field in the channel, which vindicates our earlier statement. Thus,  $E_{co}$  and  $L_{co}$  can be thought of as representing something similar to the critical values of the electric field and the channel length respectively. For electric fields comparable to or larger than  $E_{co}$ , and for channel lengths comparable to or smaller than  $L_{co}$ , the overshoot factor

cannot be neglected.

The parameter  $L_{co}$  is observed to be a function of the electron mobility  $\mu_G$ . In the analytical expression for  $L_{co}$ ,  $A$  and  $B$  have been used as fitting parameters due to the absence of any experimental data. However, the straight line fit is not accurate, as is obvious from Fig.4.7, and, thus, the extracted values of the parameters  $A$  and  $B$  may have some errors in them.

# Chapter 5

## Summary and Conclusions

The growth in VLSI has given rise to the need for developing accurate MOSFET models, which are capable of explaining device behavior down to deep submicron channel lengths adequately. Therefore, accurate MOSFET modeling has proved to be an essential step towards design and analysis of electronic circuits.

With device dimensions being scaled down, there is a corresponding increase in the drain-to-substrate leakage current  $I_{sub}$  as a function of the drain-to-source voltage, resulting from the impact ionization of high energy carriers in the surface depletion region near the drain. This current is the result of the electron-hole pair generation in this region near the drain, and is extremely sensitive to device dimensions, channel doping, terminal voltages, and temperature. An immediate consequence of this substrate leakage current is the increase in the drain-to-source output conductance  $g_{ds}$ . This parameter is very important from the analog circuit point of view, as it directly affects the amplifier gain, which uses these devices. Hence, an accurate model for  $I_{sub}$  is

necessary.

Another effect that comes into prominence with decreasing channel lengths is an abrupt increase in the device transconductance  $g_m$  for ultra-short channel length MOSFETs. Not only is this parameter of immense importance from the digital circuit point of view, but more so from the analog circuit point of view. In digital circuits, the time constant required for a MOSFET to charge a load capacitance  $C$  is proportional to  $C/g_m$ . Thus,  $g_m$  is an important factor in determining the speed of operation of digital circuits. In analog circuits, since the gain of the MOSFET amplifiers is directly proportional to  $g_m$ , any change in this parameter affects the amplifier gain. Hence, this behavior needs to be modeled adequately.

In this work, these two effects have been modeled in a semi-empirical manner. Prior to this, an existing physics based MOSFET model reported by Joardar *et al.* [8] was rederived and the results obtained from our simulation were compared with the experimental data reported [8]. A brief summary of this work is given below.

## 5.1 Summary of the work

A major drawback in the existing MOSFET models is the presence of discontinuities in the derivatives of the drain current with respect to the gate-to-source voltage and the drain-to-source voltage. These discontinuities arise primarily due to the nature of the velocity-field expressions and the smoothing functions used in the transition area between the linear and the saturation regions in these models. The model developed by Joardar *et al.* [8] attempts

to overcome the problems mentioned above. This new model is normalized surface potential based and is quasi-static in nature, i.e., the variation of the terminal voltages is assumed to be sufficiently slow, so that they can be assumed to be identical to the dc voltages at any given time. This model was simulated and the results obtained were compared with the experimental data reported by Joardar *et al.* [8].

A simple and accurate approximation of the ionization length  $l_d$  is developed in this work. This has been obtained by a calculation of the electric field distribution near the drain region. Our model results were verified with the MINIMOS simulation results reported by Wong and Poon [7], and a good correlation between the two was obtained. This new model for  $l_d$  was then used to calculate the substrate current. The results obtained from the improved substrate current model developed in this work was then compared with the experimental data reported by Arora and Sharma [6], and a good match was obtained between the two.

In this work, the abrupt increase in the transconductance  $g_m$  with decreasing channel lengths has been accounted for by proposing a new semi-empirical model for the electron mobility. The mobility has been made a function of the drain-to-source voltage, oxide thickness, gate-to-source voltage, and channel length. With large channel electric field and small channel length, the carrier mobility is bound to increase, and the increase in the transconductance is then accounted for by the correspondingly enhanced electron mobility. Our model results have been compared with the experimental data reported by Sai-Halasz *et al.* [1] and the results showed a sufficiently good match.

## 5.2 Scope for Improvement

The semi-empirical substrate current model developed in this work has expressed the maximum electric field  $E_m$  in the channel in a semi-empirical manner, with  $\eta$  and  $\beta$  being the fitting parameters. These parameters can be expressed physically as a function of the oxide thickness, substrate doping, channel length, and drain-to-source voltage. Also, there are several approximations made in evaluating the electric field  $E(y)$  as a function of the position along the channel [Eqn.(3.8)]. The Gaussian box in Fig.3.1 is assumed to extend only upto the drain-junction depth  $x_j$ , whereas in reality, the depletion region extends well beyond  $x_j$ . The electric field flux flowing from the velocity saturated region to the substrate is assumed to be negligible, and the electric field within the channel  $E(y)$  is assumed to be independent of the channel depth  $x$ . Thus, a scope for improvement exists in the accurate determination of the electric field within the channel.

In the mobility model developed in this work, the carriers taken into consideration are electrons. The same results can be extended for obtaining the new enhanced hole mobility, and, subsequently, the transconductance expression for a p-channel MOSFET. In the expression for the electron mobility developed in this work, some physical significance has been given to the parameter  $E_{co}$ , but the exact physical significance of the parameter  $L_{co}$  is not yet clear. Also, this parameter has been approximately expressed as linear function of the electron mobility  $\mu_G$  in a totally empirical manner. The future scope for improving the mobility model developed in this work lies in imparting physical significance to the parameter  $L_{co}$ , as well as obtaining a better model for  $L_{co}$  as a function of  $\mu_G$ .

# Bibliography

- [1] G. A. Sai-Halasz, M. R. Wordeman, D. P. Kern, S. Rishton and E. Ganin, "High transconductance and velocity overshoot in NMOS devices at the  $0.1 \mu m$  gate level," *IEEE Electron Device Lett.*, vol. 9, pp. 464-466, 1988.
- [2] S. Y. Chou, D. A. Antoniadis and H. I. Smith, "Observation of electron velocity overshoot in sub-100 nm channel MOSFET's in silicon," *IEEE Electron Device Lett.*, vol. EDL-6, pp. 665-667, 1985.
- [3] G. G. Shahidi, D. A. Antoniadis and H. I. Smith, "Electron velocity overshoot at room and liquid nitrogen temperatures in silicon inversion layers," *IEEE Electron Device Lett.*, vol. 9, pp. 94-96, 1988.
- [4] F. Assaderaghi, P. K. Ko and C. Hu, "Observation of velocity overshoot in silicon inversion layers," *IEEE Electron Device Lett.*, vol. 14, pp. 484-486, 1993.
- [5] J. B. Roldan, F. Gamiz, J. A. Lopez-Villanueva and J. E. Carceller, "Modeling effects of electron velocity overshoot in a MOSFET," *IEEE Trans. Electron Devices*, vol. 44, pp. 841-846, 1997.

- [6] N. D. Arora and M. Sharma, "MOSFET substrate current model for circuit simulation," *IEEE Trans. Electron Devices*, vol. 38, pp. 1392-1398, 1991.
- [7] H. Wong and M. C. Poon, "Approximation of the length of velocity saturation region in MOSFETs," *IEEE Trans. Electron Devices*, vol. 44, pp. 2033-2036, 1997.
- [8] K. Joardar, K. Gullapalli, C. McAndrews, M. E. Burnham and A. Wild, "An improved MOSFET model for circuit simulation," *IEEE Trans. Electron Devices*, vol. 45, pp. 134-148, 1998.
- [9] S. M. Sze, *Physics of Semiconductor Devices*. New York: Wiley, 1991.
- [10] S. C. Sun and J. D. Plummer, "Electron mobility in inversion and accumulation layers an thermally oxidized silicon surfaces," *IEEE J. Solid-State Circuits*, vol. 15, pp. 562-572, 1980.
- [11] Y. P. Tsividis, *Operation and Modeling of the MOS Transistor*. New York: McGraw-Hill, 1987.
- [12] Y. A. El-Mansy and A. R. Boothroyd, " A simple two-dimensional model for IGFET operation in the saturation region," *IEEE Trans. Electron Devices*, vol. ED-24, pp. 241-253, 1977.
- [13] Z. Liu, C. Hu, J. Huang, T. Chan M. Jeng, P. K. Ko and Y. C. Cheng, "Threshold voltage model for deep-submicrometer MOSFET's," *IEEE Trans. Electron Devices*, vol. 40, pp. 86-95, 1993.
- [14] M. M. Kuo, K. Seki, P. M. Lee, J. Y. Choi, P. K. Ko and C. Hu, "Simulation of MOSFET lifetime under ac hot-electron stress," *IEEE Trans. Electron Devices*, vol. 35, pp. 1004-1010, 1988.

- [15] T. Sakurai, K. Nogami, M. Kakumu and T. Iizuka, "Hot-carrier generation in submicrometer VLSI environment," *IEEE J. Solid State Circuits*, vol. SC-21, pp. 187-191, 1986.
- [16] J. Mar, S. S. Li and S. Y. Yu, "Substrate current modeling for circuit simulation," *IEEE Trans. Computer-Aided Des.*, vol CAD-1, pp. 183-186, 1982.
- [17] K. Sonoda, K. Taniguchi and C. Hamaguchi, "Analytical device model for submicrometer MOSFET's," *IEEE Trans. Electron Devices*, vol. 38, pp. 2662-2668, 1991.
- [18] J. G. Ruch, "Electron dynamics in short channel field-effect transistor," *IEEE Trans. Electron Devices*, vol ED-19, pp. 652-654, 1972.
- [19] G. Baccarani and M. R. Wordeman, "An investigation of steady state velocity overshoot in silicon," *Solid-State Electron.*, vol. 28, pp. 407-416, 1985.
- [20] T. Kobayasi and S. Kazuyuki, "Two dimensional analysis of velocity overshoot effects in ultrashort channel Si MOSFET's," *IEEE Trans. Electron Devices*, vol. ED-32, pp. 788-792, 1985.
- [21] K. K. Thornber, "Current equations for velocity overshoot," *IEEE Electron Device Lett.*, vol. 3, pp. 69-71, 1982.
- [22] M. R. Pinto, E. Sangiorgi and J. Bude, "Silicon MOS transconductance scaling into the overshoot regime," *IEEE Electron Device Lett.*, vol. 14, pp. 375-378, 1993.
- [23] K. Blotekjaer, "Transport equations for electrons in two-valley semiconductors," *IEEE Trans. Electron Devices*, vol. ED-17, pp. 38-47, 1970.

- [24] M. R. Pinto, "Simulation of ULSI device effects," in *1991 ULSI Science and Technology (Electrochem. Soc. Proc.)*, J. Andrews and G. K. Cellar, Eds., vol. 91-11, 1991, p. 43.
- [25] M. R. Pinto, W. M. Coughran, Jr., C. S. Rafferty, R. K. Smith, and E. Sangiorgi, "Device simulation of silicon ULSI," in *Computational Electronics*, K. Hess, J. P. Leburton, and U. Ravaioli, Eds. Norwell, MA: Kluwer, 1990, p. 3.

127830

127830

Date Sub

This book is to be returned on the  
date last stamped.



A127830

TH  
EE/1999/m  
K832 m